UKRAINIAN JOURNAL OF MECHANICAL ENGINEERING AND MATERIALS SCIENCE

Vol. 8, No. 2, 2022

Vinay Kumar Pal[1], Lokendra Pal Singh[2]

[1] Department of Mechanical Engineering, Sam Higginbottom University of Agriculture, Technology And Sciences Allahabad, 211007, U.P, India, e-mail: gaurishankar.vinaypal@gmail.com, ORCID: 0000-0001-7830-570X

[2] Department of Mechanical Engineering, Sam Higginbottom University of Agriculture, Technology And Sciences Allahabad, 211007, U.P, India, e-mail: vinaymd002@gmail.com, ORCID: 0000-0002-6221-8174

STUDY ON MICROSTRUCTURE CHARACTERIZATION OF FRACTURE FRONTIER OF POST WELDS HEAT TREATMENT AND TYPE IV CRACKING OF P92 STEEL WELDED JOINT

Received: April 28, 2022 / Revised: May 26, 2022 / Accepted: May 30, 2022

https://doi.org/10.23939/10.23939/ujmems2022.02.001

Abstract. In the research work presented in this study microstructure evolution at fracture frontier of crept P92 weld, creep rupture life and effect of creep exposure time on microstructure evolution in fine-grained heat affected zone were performed. Microstructure evolution and creep rupture behavior of metal arc welded joint of P92 steel plate in the as-welded have been studied. The different states of post weld heat treatment (PWHT). (i). post welded heat treatment at 760 ^{o}C for the 2h (ii). re-austenitizing at 1040 ^{o}C for 60 min and air cooled and tempering at 760 ^{o}C for 2h. In PWHT condition, most common type IV cracking was observed creep exposure 620 ^{o}C / 150 MPa. The martensitic matrix fracture is also observed in PWNT 1 condition. A move away from the fracture frontier, the cavities still remain in the microstructure while the martensitic matrix fracture is difficult to observe. The line mapping also confirmed the increase in weight percentage of Cr and Mo in $M_{23}C_6$. The elemental mapping of PWHT 2 condition is also carried out in FGHAZ which confirm the formation of Mo and Cr-rich $M_{23}C_6$ precipitates.

Keywords: leaves phase, PWHT, fracture frontier, P92 Steel, element mapping, creep rupture, microstructure

Introduction and Problem Statement

Cracks are defined on the basis of their location in weldments. The welding of P92 steel leads the formation of heterogeneous microstructure across the weldments. The different zone present in weldments shows different susceptibility to creep damage. Type I and type II crack mainly develop in the deposited weld metal, propagate either through base metal (type I) or cross over in HAZ or base metal (type II). Type III cracking occurs in CGHAZ and it can be removed by refining the grain size. In P92 welded joint, localized creep cavitation in soft zone led to intergranular fracture during the long-term creep exposure at low stress. This is termed as Type IV cracking.

From the study, it is clear that the type IV cracking mainly nucleate from the soft-zone present in weldments but it is difficult to clearly distinguish the location of the soft zone. The similar optical appearance of over-tempered base metal, FGHZA, and IC-HAZ make it difficult to distinguish the soft-zone in weldments. In a different study, over-tempered base zone, FGHAZ, and IC-HAZ have been considered as the soft zone of weldments [1–3]. The carbide coarsening and partial dissolution of precipitates in FGHAZ and IC-HAZ make it relatively soft compared to CGHAZ and weld zone. The soft zone formation leads to premature type IV cracking in FGHAZ / IC-HAZ. The type IV fracture is generally characterized as low ductility fracture because of low strain value about 10 %. Nucleation and growth of creep cavities by diffusion mechanism in FGHAZ and IC-HAZ are mainly responsible for the type IV cracking [4].

The presence of secondary phase particles at PAGBs or at the intersection of grain boundaries acts as the preferential sites for void nucleation. The coarsening of retained $M_{23}C_6$ particles was observed to be

accelerated under the creep condition. Hence, wretained $M_{23}C_6$ particles in FGHAZ/IC-HAZ acts as preferential sites for crack nucleation. Abd El-Azim et al. [5] had reported that softer martensitic matrix formation in FGHAZ/IC-HAZ, during the welding process is responsible for the type IV failure. The coarsening of precipitates and formation of Laves and Z-phase are observed to be faster in IC-HAZ compared to another zone of weldments [6,7].

A lot of works have been published on type IV cracking of P91 weldments. A limited work has been reported related to cross-weld creep test of 9–12 % Cr steels [6, 8, 9]. Type IV cracking in the cross-weld specimen was observed to be more pronounced for stress less than 100 MPa [10]. A lot of researchers have confirmed the poor creep strength of weld joint than the base metal due to premature type IV cracking [2, 5, 7, 11]. The poor strength of weld joint is attributed to the type IV failure. Watanabe et al. [7] have observed the poor creep strength of weld metal than the base metal for P91 steel weldments. Corresponding to low temperature and high stress (160 Mpa), Type I fracture was observed while decreased in stress from 160 MPa to 80/40 MPa at a higher temperature (660/650 °C), led the type IV fracture in P91 weldments. During creep, a remarkable growth of Laves and $M_{23}C_6$ phase was also reported in FGHAZ.

Abd El-Azim et al. [12] performed a comparative study on creep behaviour of P91 steel joint and base metal. The creep strength of base metal was observed to be superior to weld joint at higher creep exposure temperature about 650 °C while at a lower temperature about 600 °C, it approached to creep strength of the base metal. Fracture location was observed in the base metal near to HAZ for short-term creep exposure (426 h) at 600 °C and high applied stress of 150 MPa. The lower applied stress for same applied temperature was resulted in shifting of fracture location and type IV fracture occurred in FGHAZ of the weld joint. Laha et al. [2] reported the soft zone formation in IC-HAZ of P91 joint and type IV fracture was also associated with IC-HAZ.

P92 steel joint exhibited the lower creep rupture strength than thebase at higher exposure temperature and lower applied stress while at low temperature and high applied stress higher creep strength of base metal was observed.The fracture behaviour of the P92 joint was observed to be similar as reported by Abd El-Azim [12].For low temperature and high applied stress, fracture location was observed in the base metal near to HAZ. The fracture location was observed to be shifted from base metal to IC-HAZ for lower applied stress at higher exposure temperature. Albert et al. [13] have also studied the effect of PWHT duration on type IV cracking nature in P122 weld joints. The creep test was performed at 650 °C for 70 MPa. PWHT duration was varied from 15 min to 4 h but no any significant change was observed in creep rupture time and fracture behaviour. In all the cases, type IV fracture was observed. Sawada et al. [14] have studied the cross-weld long-term creep behaviour of E911 joint at 600 ^{o}C.The fracture was noticed in soft FGHAZ. The growth of $M_{23}C_6$ in FGHAZ was observed faster than the base metal. The Z-phase formation was observed both in FGHAZ and base metal FGHAZ exhibited higher number density of Z-phase than the base metal. For long-term creep exposure at the low level of stress, creep life was observed to be minimum in FGHAZ[10].

The type IV cracking in P91 weld joint results in a reduction in cross-weld creep strength during the long term creep exposure. Researchers have proposed various techniques such as normalizing/tempering treatment, adjusting welding procedure and modifying tempering treatment to enhance the cross-weld creep strength of P91 weld joint [2, 4, 10].

As discussed above, heterogeneity across the weldments are mainly responsible for the type IV cracking. PWHT leads the recrystallization that enhances the non-uniform distribution of precipitates and also reduces the heterogeneity presented across the weldments. To enhance the cross-weld creep strength of the P92 joint, PWHT was observed to be not so effective. To remove the heterogeneity across the sub-zone of P92 welded joint, the entire weldments needs to be renormalized. Renormalizing of welded component leads the formation of homogeneous microstructure and alleviates the premature type IV cracking. Mitsubishi Heavy Industries in Japan have successfully implemented the N&T of P92 weldments and observed little or no difference in creep behaviour of cross weld P92 weld joint and base metal for creep exposure time up to 30000 h and temperature of

700 ^{o}C [15]. However, in actual practice, N&T treatment of long welded components is not possible. Local normalizing might be the cause of secondary soft zone formation.

Half-tempered weld joint has reported a superior creep strength than conventional weld joint for short-term creep test [16]. The half-tempering technique utilized the partial tempering of base metal before the welding and completes the tempering as PWHT. The effect of heat input and preheat temperature on type IV cracking behaviour have been reported by Francis et al. [17]. A narrow HAZ formation is also expected to enhance the creep rupture life of cross-weld specimen [8]. A P92 welded joint with narrow HAZ results in lower creep cavitations in a soft zone and minimize the tendency of type IV cracking. The addition of elements like B and W in parent metal composition might be useful to enhance the creep rupture strength of welded joint [18].

Manugula et al. reported a uniform hardness across the weldments and almost similar to base metal as a result of PWNT treatment. The PWNT treatment resulted in complete elimination of δ-ferrite from weld fusion zone that led to higher Charpy toughness of fusion zone. However, only a few studies have reported the effect of re-austenitization (normalizing) followed by tempering treatment (PWNT) of P91 weldments and its effect on microstructure evolution. The combined effect of different heat treatments on creep rupture behavior is not readily available in the literature. [19]

The aim of present investigation is to tempering heat treatment and subsequent post weld heat treatment and characteristic of short -term creep behavior and fracture frontier of the creep.

Main Material Presentation

Multi-pass welding

The bevel angle, root face height and root gap were 37.5°, 1.5 mm and 1.5 mm, as shown in Fig. 1, *b*. The plates were preheated at 300 °C before the welding. To minimize the distortion, the plate was tack welded from both sides, as shown in Fig. 1, *c*. The root pass was carried out using the GTAW process with AWS ER90S-B9 (9CrMoV-N) filler wire of diameter 1.6 mm for all the welds. Fig. 1, *d* and *e* shows the plates after root pass on top and a bottom side, respectively. SMAW process was used for filling pass using the welding consumable rod of diameter 4 mm and designated as 9CrMoV-N (AWS E9015-B9). The plate after complete welding is shown in Fig. 1, *f*. For the case I, the welding process parameters used for the GTAW root pass (top and bottom side) and SMAW filler pass are depicted in Table 1. The heat transfer efficiency is considered 0.60, 0.80 for root pass (GTAW) and filler pass (SMAW), respectively.

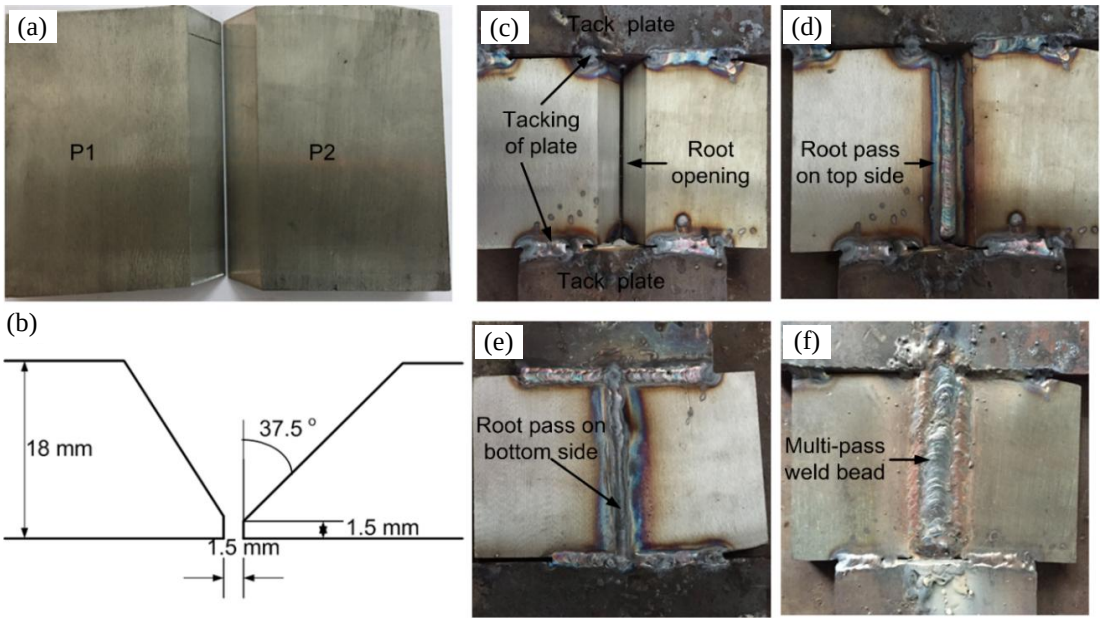

Fig. 1. (a) Machined and grooved plate, (b) Groove design, (c) Plate after tacking, (d) After root pass on top side, (e) After root pass on bottom side and (f) Plate after completion of filling pass

The welding was carried out in four different conditions of weld consumable as depicted in Table 1. The number of filler passes used for the welding for the case I, case II, case III and case IV were 14, 13, 14 and 14, respectively. After the completion of welding, the weld joints were subjected to post-weld heating at a temperature of 280 °C for 60 min. The one weld joint for different diffusible hydrogen level was allowed to cool down to room temperature after the post-weld heating. The second one from each condition was subjected to subsequent PWHT. The third weld joint from each condition was allowed to N&T heat treatment. The PWHT temperature range recommended is below than the critical temperature (Ac1≈ 815 °C). For large size specimen, the PWHT temperature was recommended less than A_{c1} by 10–20 ^{o}C[20]. The N&T were carried out at 1050 ^{o}C/40min and 760 °C /2h, respectively.

Table 1

Welding process parameters for root pass and filler pass

Sample 1	Current (amp)	Voltage (volt)	Time (sec)	Travel speed (mm/sec)	Efficiency (η)	Heat input (kJ/mm)
Root pass 1	115–120	14–16	70	2.14	0.60	0.494
Root pass 2	110–115	12.0–14.0	70	2.14	0.60	0.410
1	140	22.0–23.0	45	3.20	0.80	1.177
2	144	21.6–22.8	44	3.40	0.80	1.195
3	144	22.5–23.6	28	5.36	0.80	1.240
4	144	21.8–23.3	33	4.55	0.80	1.213
5	144	22.8–23	39	3.85	0.80	1.232
6	144	21–22.8	35	4.29	0.80	1.178
7	144	21–23	35	4.29	0.80	1.184
8	144	21.5–23	36	4.17	0.80	1.197
9	144	21.5–23	30	5.00	0.80	1.197
10	144	21–23	31	4.84	0.80	1.184
11	148	23.3–24	40	3.75	0.80	1.308
12	151	22–25.6	30	5.00	0.80	1.343
13	151	22–24.5	30	5.00	0.80	1.312
14	151	21.2–24	29	5.17	0.80	1.275

Transverse creep test samples were prepared toform the previously welded P92 plate. The root pass was carried out using the GTAW process with AWS ER90S-B9 (9CrMoV-N) filler wire of diameter 1.6 mm while shielded metal arc welding (SMAW) process was used for filling pass using the welding consumable backed rod of diameter 4 mm and designated as 9CrMoV-N (AWS E9015-B9). The baking of electrode was carried out at 250 °C. The detailed welding process is Multi-pass welding. For root pass, arc thevoltage varied in therange of 12–16 Volts while welding currentwas maintained in therange of 110–120 amp. For filling passes welding current varied from 140 to 150 amp while arc voltagewas maintained in therange of 21–25 Volts. Creep tests were performed in open air condition at 620 °C for a stress level of 150 MPa and 200 MPa. The dimensions of the creep test specimen are given in Fig. 2. The creep test was conducted in three different conditions of heat treatment as discussed in Table 2.

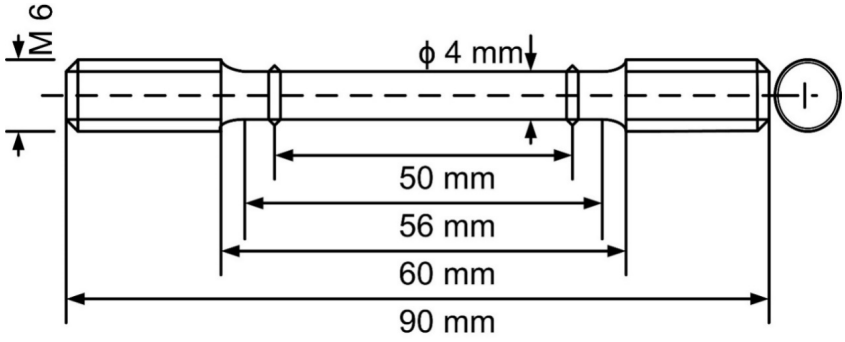

Fig. 2. Schematic of creep test specimen for weld metal

Table 2

Creep tests condition for P92 welds joint

Creep test condition	Applied stress (MPa)	Temperature (^{o}C)
As-welded 1	120	620
As-welded 2	150	620
PWHT 1	120	620
PWHT 2	150	620
PWNT 1	120	620
PWNT 2	150	620

In post weld heat treatment (PWHT) condition, the welded plate subjected to post weld heat treatment at atemperature of 760 ^{o}C for 2h. In post weld normalizing and tempering (PWNT) condition, welded plate subjected to normalizing at a temperature of 1040 ^{o}C for 60 min and air-cooled and tempered at 760 ^{o}C for 2 h, followed by air cooling.

Microstructure characterization of crept sample

In order to characterize the crept sample of base and weld metal (from the gauge and gripping area), the samples were polished by using series of SiC grit paper from 120 to 2000 micron. The paper polishing was followed by cloth polishing using alumina powder to obtain a mirror finished surface. The polished samples were subsequently etched with Vilella's reagent (1g of picric acid +5 mL of hydrochloric acid +100 mL of ethyl alcohol). The etched samples were characterized by using the FESEM microscope. For FESEM, SEMQUANTA 200 Field scanning electron microscope was utilized with accelerating voltage and probe current of 20 kV and 10 nA, respectively for 8 mm working distance. Omnitech-S. Auto-equipped with a digital camera and software was utilized for microhardness measurement at aload of 500 g with a dwell time of 10 s. The precipitate size and its distribution in gauge and gripping area of the crept sample were measured using Image J software.

Results and Discussion

Creep deformation and rupture behaviour of weld joints

The fractured creep specimen and their rupture life are given in Fig. 3 and Table 3, respectively. In as-welded condition and at 620 ^{o}C creep exposure temperature, creep rupture life were measured 100 h and

950 h for the applied stress of 200 MPa and 150 MPa, respectively. In case of high applied stress and short creep exposure condition, fracture occurs in the base metal. For rupture time of 1000 h, typical type IV cracking is noticed and fracture location shifted from the base metal to soft FGHAZ, as shown in Fig. 3. The rupture that generates the crack in base metal only is referred as type V crack [21]. After the PWHT, fracture location is noticed in FGHAZ for applied stress in the range of 150-200 MPa, as shown in Fig. 3. PWHT of welded joint results in a significant increase in creep rupture life as compared to as-welded condition for the high applied stress of 200 MPa and creep exposure temperature of 620 ^{o}C. The creep rupture life increases form 100 h to 322 h. However, the low applied stress of 150 MPa leads to poor creep rupture life of the PWHT welded joint as compared to as-welded condition and it decreases from 1000 h to 346 h. The specimen that fractured from HAZ shows type IV cracking for both as-welded and PWHT condition.

In PWNT condition, the uniform microstructure and hardness were reported across the welded joint of P92 steel. For applied stress of 200 MPa (PWNT 1), creep rupture life of transverses P92 welded joint was measured to be higher than as-welded 1 and PWHT 1 condition. In PWNT 1 state, creep rupture life is measured 44.72 % more than that of PWHT 1 and 33.14 % than that of PWHT 2 condition. For low applied stress (150 MPa) and same operating temperature (PWNT 2), creep rupture life was measured 2432 h. The creep rupture life in PWNT 2 condition is measured 594.89 % higher than PWHT 2 condition and 142.7 % higher than as-welded 2 conditions. In PWNT conditions, the fracture location is noticed in base metal (Type V) as a result of uniform structure across the welded joint. For PWNT condition, the fracture location is reported in Fig. 3. Hence, PWNT of the P92 weldments instead of subcritical PWHT provides the uniform microstructure across the welded joint, as well as much higher, creep rupture life. PWNT improves the creep rupture life of the welded joint as well as shift the fracture location from soft FGHAZ/IC-HAZ to base zone. To locate the fracture location, macrostructure is shown in Fig.3. For detail microstructure characterization, samples were removed from the fractured specimen and mounted in epoxy resin, as shown in Fig. 3.

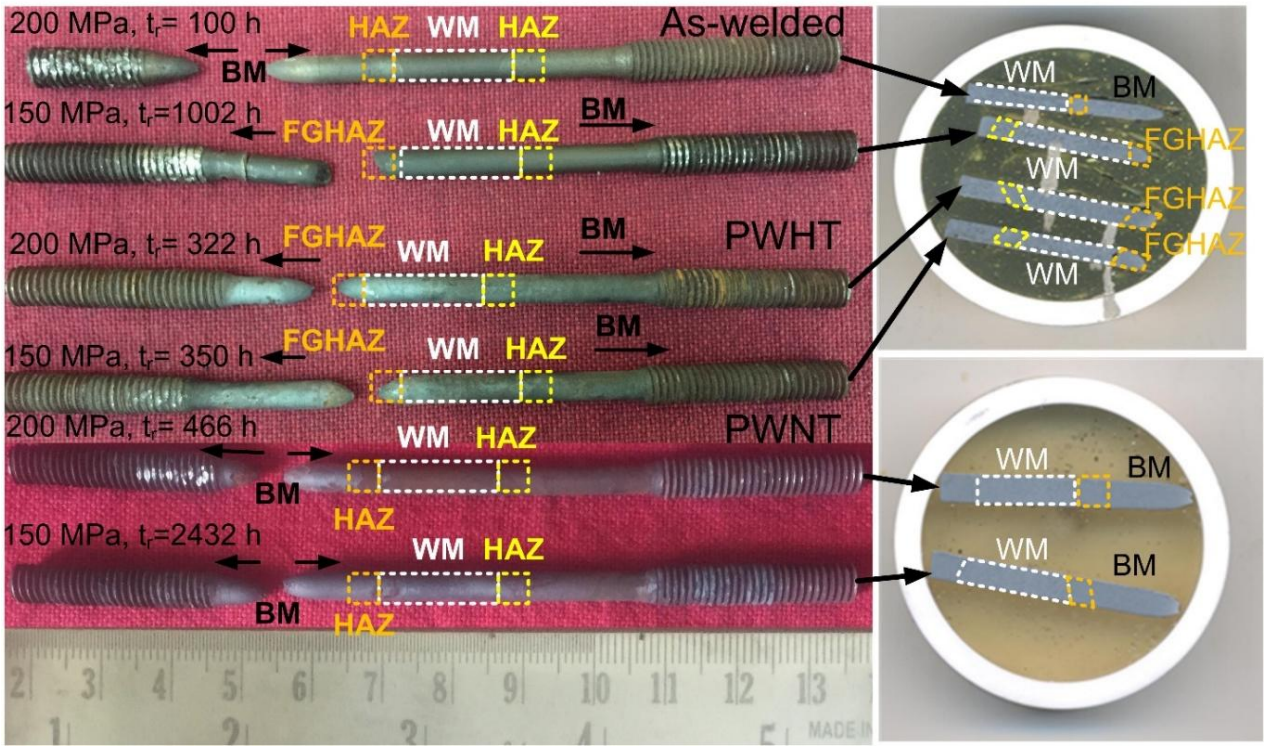

Fig. 3. Fractured creep tested specimen with fracture location and creep exposure time

Table 3

Creep test results for weld joints

Creep test condition	Applied stress (MPa)	Temperature (^{o}C)	Creep exposure time (h)	Min creep rate ($h^{-1)}$	Fracture location
As-welded 1	200	620	100	2.30×10^{-2}	BM
As-welded 2	150	620	1002	8.71×10^{-4}	FGHAZ
PWHT 1	200	620	322	9.16×10^{-3}	FGHAZ
PWHT 2	150	620	350	5.88×10^{-3}	FGHAZ
PWNT 1	200	620	466	3.66×10^{-3}	BM
PWNT 2	150	620	2432	6.79×10^{-4}	BM

The creep curves of P92 weld joints under different operating conditions and corresponding to different applied temperature and stress are shown in Fig. 4, *a–b*. Typical creep curve for PWHT 1 condition is depicted in Fig. 4, *c*. The creep curved exhibit small instantaneous strain on loading, a transient primary stage, secondary steady-stage and prolonged accelerating ternary stage. It is difficult to distinguish the primary creep stage for the lower level of applied stress (150 MPa), as shown for PWNT 2 and PWHT 2. Longer secondary creep stage is clearly observed for the lower level of applied stress at 620 ^{o}C of creep exposure (PWNT 2 and PWHT 2). A longer secondary creep stage is also observed for PWNT 1 condition. For applied stress of 200 MPa, maximum percentage elongation is observed for PWHT 1 and minimum for as-welded 1. In the low level of applied stress (150 MPa) for same creep exposure temperature, PWNT 2 condition produces the maximum elongation. The minimum creep rate variation with applied stress is given in Fig. 4, *d*. The minimum creep rate increases with increase in applied stress, as shown in Table 4. The minimum creep rate ($\dot{\varepsilon}_s$) variation with applied stress followed Norton's power law of creep ($\dot{\varepsilon}_{min} = A\sigma^n$). The variation in stress component (n) refers to change in creep deformation mechanism of the materials [22]. For Harper-Dorn creep, stress component (n)=1 is considered. In Harper-Dorn creep, the dislocation density is invariant with the applied stress. The value (n)=3 is taken for the Solute-drag creep where the rate of migration of solute atoms control the moving dislocations. In case of a dislocation climb controlled process, the value of stress component (n)=5. Dislocation climb controlled mechanism occurs in the materials which show sub-grain formation and power-law breakdown (PLB) behaviour [22]. The stress component is considered as 8 for the dislocation climb controlled mechanism in which microstructure remain constant during the creep exposure. In the present investigation, the n value of 11, 2 and 6 have been observed for as-welded, PWHT and PWNT condition. The lowering in n value is observed mainly due to excessive microstructure change at a hightemperature such as coarsening of $M_{23}C_6$ precipitates, Laves phase formation and a decrease in coherent strain between the matrix and fine V and Nb-rich MX precipitates [23, 24].

For different creep exposure condition, the variation of strain rate with creep exposure time is shown in Fig. 5, *a–f*. The pronounced ternary stage of creep deformation is clearly observed in Fig. 5. In primary stage of creep regime, creep rate decreases significantly with creep exposure time and followed by the region of minimum creep rate. After the steady-state creep stage, faster rate of creep deformation is observed in tertiary stage till the fracture of the specimen. The P92 welded joints spent the majority of rupture time in the tertiary stage for each condition except the PWNT 2 condition. In primary transient creep stage, the decrease in strain rate is attributed to the work hardening behaviour of material as a result of multiplication and interaction of the dislocations. After the certain period of the time, work hardening and recovery mechanism reach the equilibrium state and leads to constant strain rate due to dislocation annihilation and rearrangement. In the last stage, coarsening of precipitates and growing creep cavities accelerate the creep rate [25].

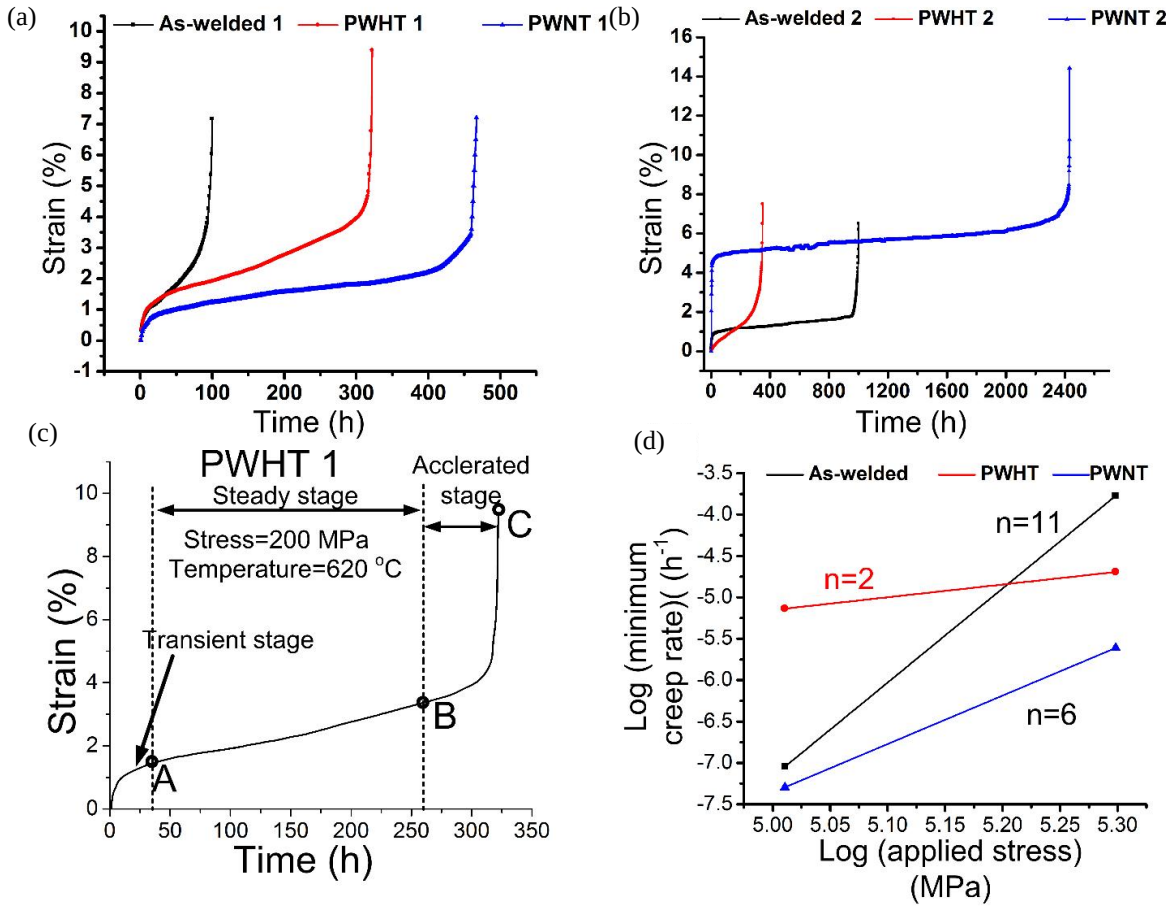

Fig. 4. (a) Creep curves for as-welded, PWHT and PWNT condition at (a) 620 °C/200 MPa, (b) 620 °C/150 MPa, (c) creep curves at a temperature of 620 °C and a stress of 200 MPa (PWHT 1) with the three dominant stages (Transient, steady, and accelerated stage) and (d) stress dependence of minimum creep rate at 620 °C

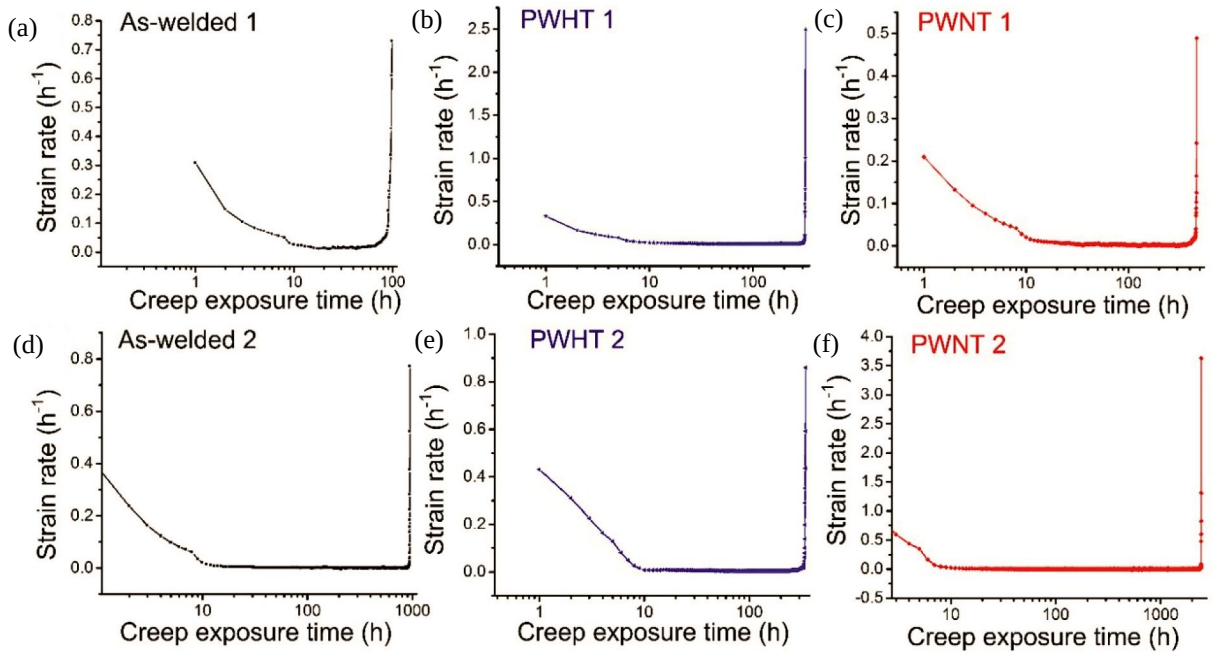

Fig. 5. Variation in creep rate as a function of creep exposure time and heat treatment condition (a) as-welded 1, (b) PWHT 1, (c) PWNT 1, (d) as-welded 2, (e) PWHT 2 and (f) PWNT 2

The minimum strain rate is observed to be increased with increase in applied stress for each condition, as given in Table 4. The elongation to failure and reduction in area for each case is depicted in Table 4. The creep specimens are fractured in a ductile manner with external necking. In as-welded and PWHT condition, the % reduction in the areais measured to be more than 90 %. In PWNT 1 and PWNT 2 condition, the percentage reduction in the areais measured to be 83.47 % and 88.6 % respectively. The percentage reduction in the areais measured to be higher for the stress of 150 MPa as compared to 200 MPa. The % elongation is also reported in Table 4. In as-welded and PWHT condition, percentage elongation is measured to be higher for the applied stress of 200 MPa, but in PWNT condition, maximum percentage elongation is measured for the applied stress of 150 MPa.

Table 4

Reduction in area (%) and elongation (%) for different creep test conditions

Creep test condition	Reduction in area (%)	Fracture elongation (%)
As-welded 1	91.38	7.16
As-welded 2	93.87	6.5
PWHT 1	92.08	9.38
PWHT 2	93.75	7.5
PWNT 1	83.47	7.2
PWNT 2	88.6	14.43

Microstructure characterization of optical micrograph in fracture frontier

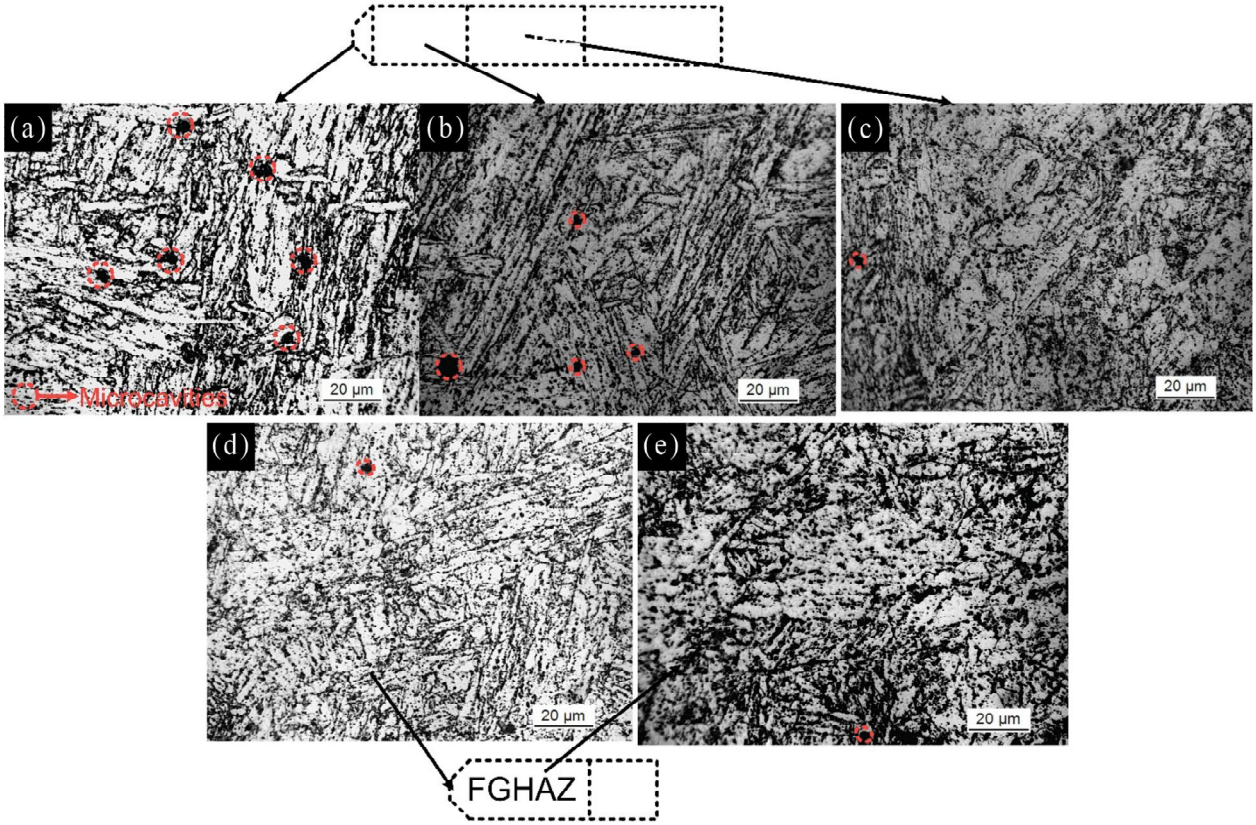

Fig. 6. Optical micrograph in as-welded condition (a), (b) and (c) for as-welded 1 condition at fracture frontier, 3 mm away from fracture frontier and FGHAZ, respectively; (d) and (e) for as-welded 2 conditions at fracture frontier and FGHAZ

The nearest area of the crack tip is denoted as the fracture frontier, as shown in thetop of the Fig. 6. In as-welded 1 condition, fracture occurs in over tempered base zone. The fracture frontier of the crept

sample is shown in Fig. 6, *a*. A number of microcavities are clearly observed in the nearest area of the tip. The microstructure in fracture frontier zone consists of coarse lath blocks with precipitates along it. As themove away from the fracture frontier but within the base zone, the number of creep cavities is observed to be reduced, as shown in Fig. 6, *b*. The microstructure shows the fine lath blocks as compared to fracture frontier zone. In FGHAZ, almost negligible microcavities are observed. The lath blocks are trace by the precipitates as observed in black dotted form. In as-welded 2 condition, the fracture occurs in the FGHAZ. The fracture frontier observed in FGHAZ instead of the base zone. Both fracture frontier and FGHAZ are characterized by lath blocks, precipitates and a negligible amount of microcavities. However, in FGHAZ, ahigherdensity of precipitates are observed along the lath blocks. From the optical micrograph, it is difficult to trace the prior austenite grain boundaries (PAGBs) as a result of grain coarsening.

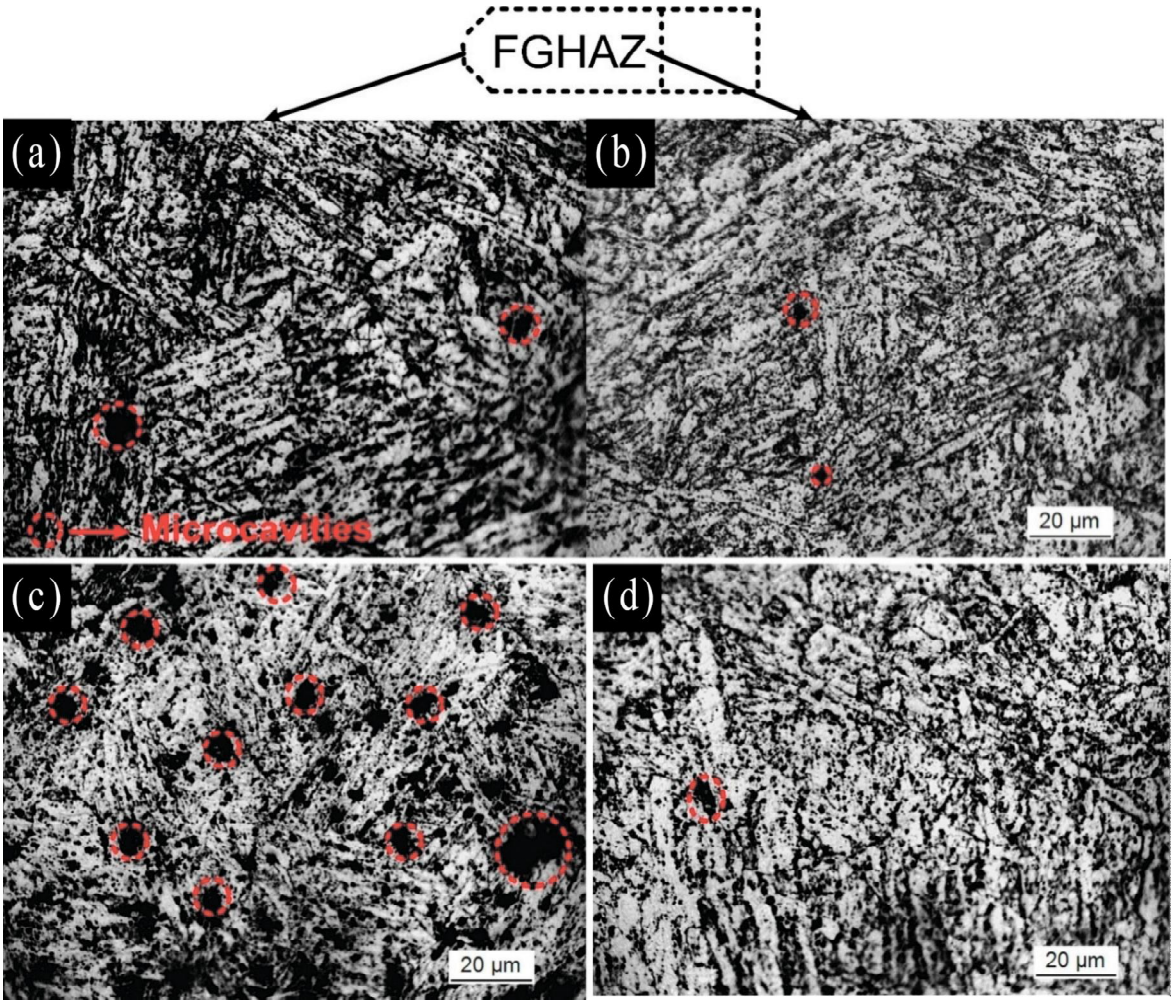

Fig. 7. Optical micrograph in PWHT condition (a), and (b) and (c) for PWHT 1 condition at fracture frontier, and FGHAZ, respectively; (c) and (d) for PWHT 2 condition at fracture frontier and FGHAZ

The micrograph of fracture frontier for PWHT condition is shown in Fig. 7. In PWHT condition, failure occurs in the FGHAZ zone. Hence, fracture frontier exists in FGHAZ for both low and high applied stress in PWHT condition. For a high level of applied stress (PWHT 1), fracture frontier shows the microcavities beside the martensitic lath blocks. In FGHAZ (2 mm away from the fracture frontier), fine lath blocks with fewer microcavities are observed. For low level of applied stress, higher creep rupture life leads to the formation of higher density of microcavities at fracture frontier, as shown in Fig. 7, *c*. The creep cavities are generally observed along the lath blocks. In FGHAZ (2 mm away from the fracture frontier), almost negligible microcavities are observed, however, coarsening of lath blocks are clearly observed.

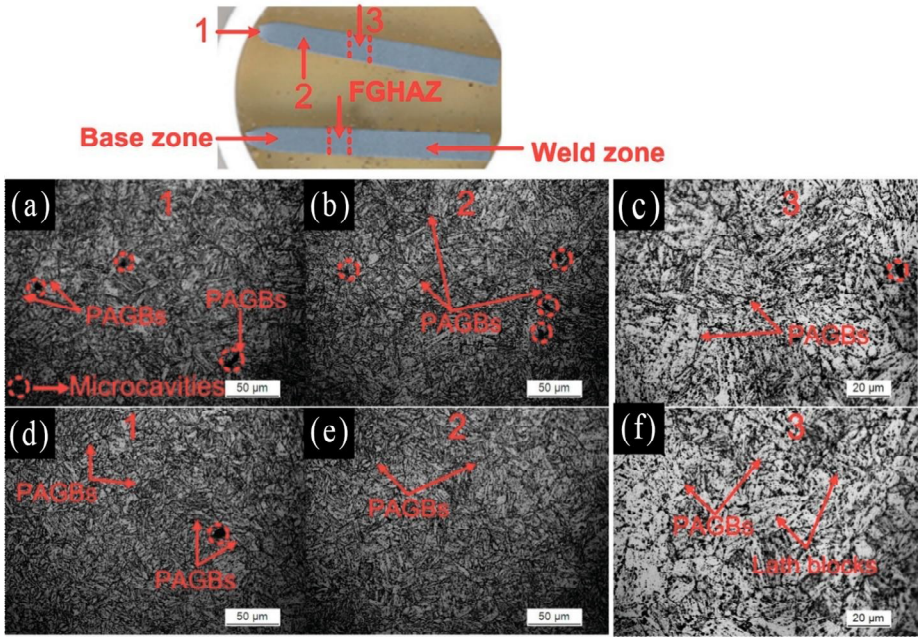

Fig. 8. Optical micrograph in PWNT condition (a), (b) and (c) for PWNT 1 condition at fracture frontier, 3 mm away from fracture frontier and FGHAZ, respectively; (d), (e) and (f) for PWNT 2 condition at fracture frontier 3 mm away from fracture frontier and FGHAZ, respectively

In PWNT condition, a micrograph of fracture frontier and FGHAZ is shown in Fig. 8. In PWNT condition, fracture occurs in the base zone as much away from the FGHAZ as a result of homogenization of microstructure. For a high level of applied stress at 200 MPa at 620 ^{o}C (PWNT 1), the microstructure of fracture frontier is shown in Fig. 8, *a*. The creep cavities are observed along the PAGBs. The martensitic matrix fracture is also observed in PWNT 1 condition. A move away from the fracture frontier, the cavities still remain in the microstructure while the martensitic matrix fracture is difficult to observe. The cavities are observed along the PAGBs as a result of the higher density of coarse precipitates which acts as the stress raiser sites. At fracture frontier and 3 mm away from the fracture frontier, the PAGBs and lath blocks are clearly observed while in FGHAZ, it is difficult to trace the PAGBs, as shown in Fig. 8, *c*. The coarse lath blocks with precipitates are observed in FGHAZ. The lath blocks and PAGBS are traced by the precipitates. In PWNT 2 state, a negligible amount of creep cavities are observed in fracture frontier zone Fig. 8, *e*. However, the microcavities are observed along the PAGBs as a result of coarse precipitates. As one moves away from the fracture frontier, the microstructure is characterized by PAGBs and lath blocks. The microcavities are not observed in the martensitic microstructure. For PWNT 2 condition, FGHAZ is characterized with PAGBs which are traced by the precipitates and lath blocks with precipitates, as shown in Fig. 8, *f*. For further characterization of the fracture frontier to confirm the precipitates, SEM study was performed as discussed below.

Crack-tip

The evolution of creep damage in different creep exposure conditions is shown in Fig. 9–13. The fracture of creep exposed specimen occurs in form of creep cavities and microcracks. Fig. 9 shows the micrograph of the creep ruptured specimen for an as-welded sample at the frontier at 620 °C under 200 MPa. At the fracture frontier, the microcavities are clearly observed, as shown in Fig. 9, *a*. The cavities form due to stress raiser near the precipitates that acts as a barrier for dislocation movements. At a higher magnification Fig. 9, *b*, it can be seen that the microcavities form along the prior austenite grains. The martensite fracture is clearly shown in Fig. 4, *b*. The martensite fracture is generally observed due to the martensite lath break up. The higher magnification micrograph Fig. 9, *d* confirms the nucleation of spherical cavities at the PAGBs as a result of deformation mismatch and leads to the formation of microcavities. The microcavities within the martensite laths grow and connect to each other under the creep deformation, resulting in martensite fracturing. Fig. 9, *c* shows another region of the crack frontier free from the creep cavities. The lath blocks and accumulation of precipitates along lath blocks are clearly

observed. The coarsening of these precipitates might also act as creep cavities. Fig. 9 shows the fracture frontier of the crept sample for PWHT 1 condition. The crack pattern is observed to be similar to as-welded 1 condition. The creep cavities are shown at the fracture frontier in Fig. 9, *a*. The cavities are observed in a spherical shape. The martensite fracturing is also observed along PAGBs in higher magnification micrograph of Fig. 9, *b*. The martensite fracturing occurs perpendicular to the direction of the laths martensite. The creep cavities are observed to grow along the stress direction. The spherical shape creepscavities is shown in Fig. 9, *c*. The creep cavities are observed to be surrounded by the precipitates. The cavities free region of the crack frontier is shown in Fig. 9, *d*. The microstructure shows the presence of coarse precipitates having cylindrical and spherical shape and fine precipitates of spherical shape. The size of spherical shape coarse precipitate varies from 475 to 504 nm. The length and width of cylindrical shape particle are observed in the range of 390–461 nm and 150–222 nm, respectively. The fine spherical particles are observed in the range of 50–120 nm. Fig. 10 shows the fracture frontier of the crept sample for PWNT 1 condition. In PWNT 1 condition, a higher number of creep cavities can be seen as compared to as-welded 1 and PWHT 1 condition. The size of cracks is also observed to be higher than the as-welded and PWHT condition. The higher amount of creep cavities in PWNT specimen suggests that cavities play an important role in determining the creep rupture life. At low magnification both microcavities and microcracks are observed at the surface-red arrow shows to microcracks and yellow point to microcavities, as shown in Fig. 10, *a*. The cavities are formed due to the hindering effect of precipitates that results in high-stress raiser near the precipitates. The martensite cracking is characterized by the presence of thin cracks, referred as microcracks that generally occur along the lath boundaries [26]. The hardness and brittleness of lath martensitic microstructure make sliding of the martensitic lath boundaries difficult, which results in microcracks nucleation under high applied stress [27]. The detailed view of the creep cavities is shown in Fig. 10, *b–c*. The continuous microcavities along the lath boundaries are shown in Fig. 10, *c*. Theses microcavities will grow and connect to each other under creep deformation. The bigger size microcavities along the martensitic lath direction are shown in Fig. 10(*d*). The microcracks and microcavities are observed to grow parallel to the direction of the loading. In fracture frontier mainly two types of the microcracks are observed: one is martensite cracks that related with stress concentration or deformation mismatch along two martensitic laths. Another one is martensite fracture that related tomartensite laths break up.

Fig. 11 shows the microstructure of fracture frontier crept at 620 ^{o}C under 150 MPa (as-welded 2). For higher creep rupture life (as-welded 2), the number density of creep cavities is significantly higher as compared to lower creep rupture life (as-welded 1). A fewer amount of microcracks are also observed, as shown in Fig. 11, *a*. The detailed view of creep cavities is shown in Fig. 11, *b*, *c*. The detailed view of fracture surface clearly shows the formation of spherical shape creep cavities along the PAGBs and lath boundaries. The cavity formation might be due to coarse $M_{23}C_6$ precipitates located along the lath boundaries and PAGBs, as shown in Fig. 11, *d*.

For PWHT 2 condition, a micrograph of fracture frontier is shown in Fig. 12. A significantly fewer number of microcavities and negligible microcracks can be seen as compared to PWNT 1. The fracture frontier is appeared to be similar to PWHT 1 and as-welded 2 conditions. The detailed view of spherical creep cavities is shown in Fig. 12, *b–d*. Fig. 12, *b*, *c* show the formation of creep cavities along the PAGBs. The detailed view of Fig. 12, *c* shows the accumulation of precipitates around the microcavities. The agglomeration of precipitates is also observed near the microcavities, as shown in Fig. 12, *d*. The precipitates are considered as the coarse $M_{23}C_6$ type carbides. The generation of creep cavities along the lath and prior austenite grain boundaries are attributed to higher stress concentration and presence of coarse precipitates. The fracture frontier of the crept specimen for PWNT 2 condition is shown in Fig. 13. A significantly greater number microcracks and microcavities can be seen as compared to the as-welded and PWHT condition in Fig. 13, *a*. However, the fracture frontier looks similar to PWNT 1 condition. At a low level of stress and high creep rupture life (PWNT 2), the number density of microcracks and microcavities are observed to be higher as compared to the high level of applied stress and low rupture life (PWNT 1). The elongated cavities along the direction of stress are shown in Fig. 13, *b*. A continuous microcavities formation within the martensitic laths is shown in Fig. 13, *c*. Fig. 13, *c* shows the nucleation of microcavities at the lath boundaries in the direction of martensitic laths. This occurs as a result of

deformation mismatch and leads to initiation of microcavities. The martensite fracture is also shown in Fig. 13, *c–d*. In Fig. 13, *d*, microcavities formation due to the coarse precipitates can be seen. In PWNT 2 condition, the formation of Laves phase is also observed as reported later. The bigger size Laves phase also helps to initiate the microcavities. In PWHT and as-welded conditions, fewer parentages of microcavities and microcracks are observed at the fractured frontier. In PWNT condition, bigger size of precipitates is observed along the lath boundaries and packet boundaries as discussed earlier. The bigger size precipitates might act as stress raiser sites for the crack nucleation. In PWNT 2 condition, the hard and brittle Laves phase is also responsible for the nucleation of creep cavities.

From the analysis of the fracture frontier, it is concluded that the creep cavities are observed along the triple boundaries among the martensitic laths. Fig. 9, *a–d*, Fig. 10, *b*, Fig. 10, *c*, Fig. 11, *b* and Fig. 12, *c* and Fig. 13, *c* show the creep voids formed at triple boundaries which is consider as the grain boundaries between PAGBs and martensitic lath boundaries.

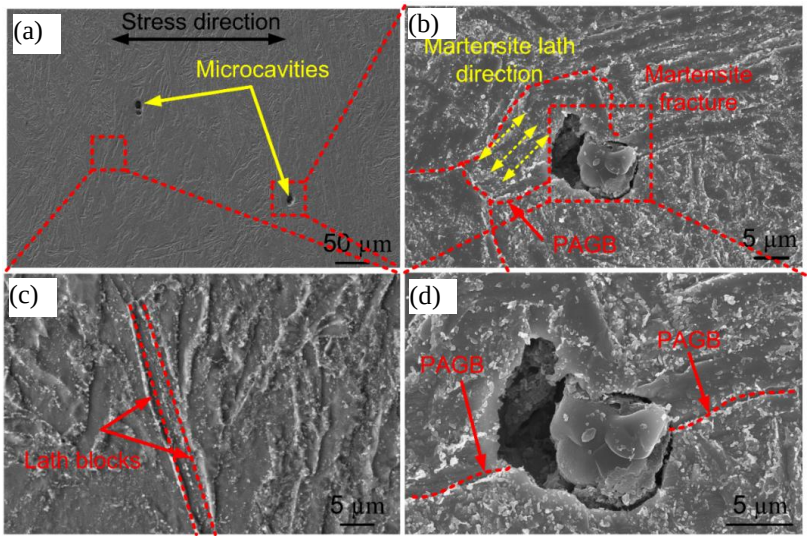

Fig. 9. Damage incurred in as-welded 1 condition during creep deformation at fractured frontier: (a) at low magnification of 500x, (b) martensite fracture within martensite laths, (c) crack frontier area free from the creep cavities in (a), (d) high magnification

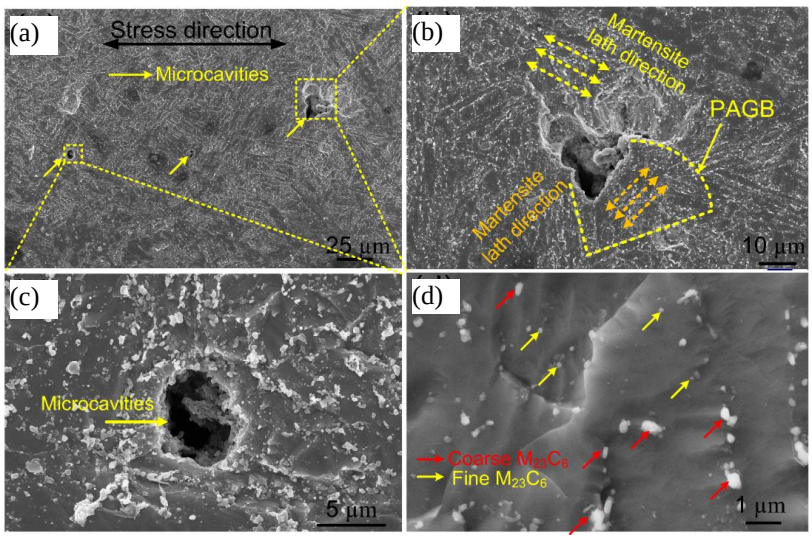

Fig. 10. Damage incurred in PWHT 1 condition during creep deformation at fractured frontier: (a) at low magnification of 1000x, (b) martensite fracture within martensite laths and martensite cracking along lath boundaries, (c) detailed view of selected area in (a), (d) area of crack frontier free from creep cavities

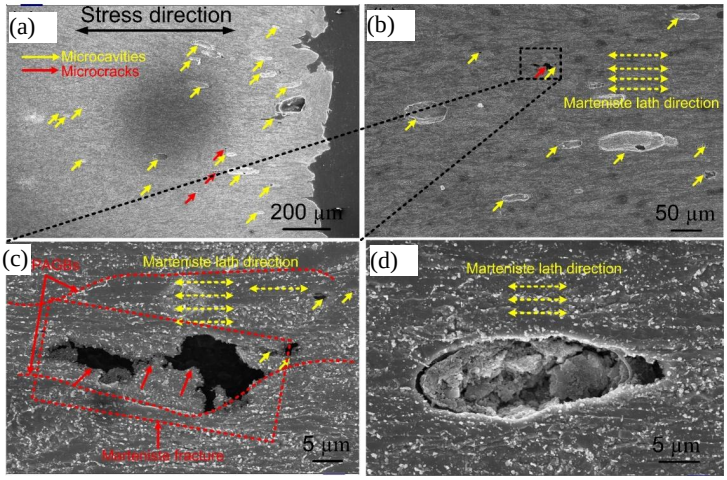

Fig. 11. Fracture frontier forPWNT 1 condition: (a) macroscopic view of cross-section, (b) elongation of creep cavities along loading direction (c) martensite fracture within martensite laths and martensite cracking along PAG boundaries in direction of martensitic laths and (d) creep cavities along lath martensitic direction

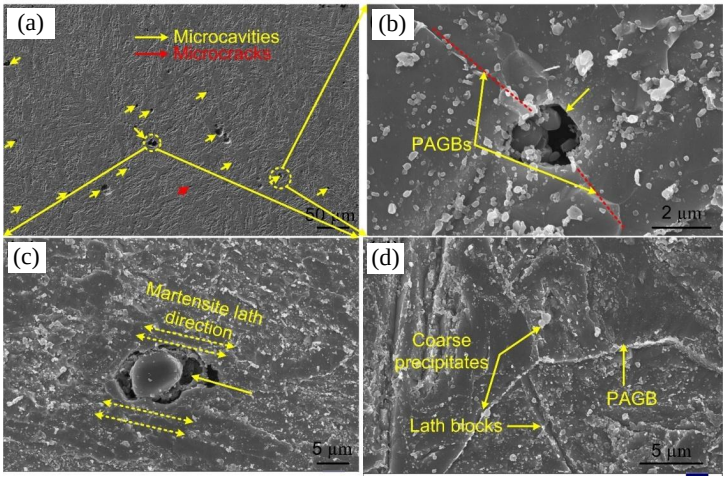

Fig. 12. Fracture frontier for as-welded 2 condition:
(a) at low magnification of 500x, (b) creep cavities formation along the PAGBs (c) creep cavities formation along the lath boundaries and (d) coarse precipitates formation lath and PAG boundaries

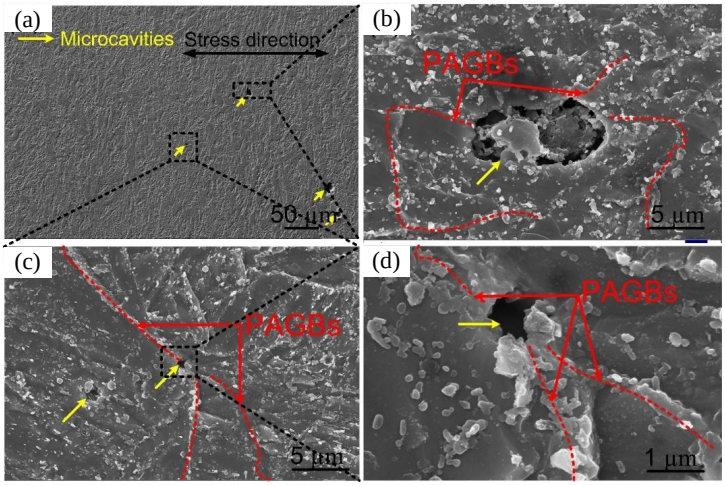

Fig. 13. Damage incurred in PWHT2 condition during creep deformation at fractured frontier:
(a) at low magnification of 500x, (b) microcavities along PAGBs in detailed view (c) microcavities along PAGBs at different location, (d) agglomeration of precipitates along the microcavity

The creep voids in soft zone of HAZ of P92 welds joint is generally formed as a result of stress concentration that leads to the Type IV failure [28]. The higher concentration is generally reported at the interface of coarse $M_{23}C_6$ or Laves phase and soft matrix [29]. Hence, the interface between coarsened $M_{23}C_6$ and Laves phase and soft matrix acts as the higher concentration sites and leads to creep voids nucleation at the interface. The triple boundaries also act as the higher concentration sites and facilitate the nucleation of creep voids. The schematic nucleation of creep voids at triple boundaries is shown in Fig. 14, *e*. The higher stress at that location results in grow of voids and connect into cracking. Finally the propagation of cracking results in final fracture of the welded joint.

The detailed view shows the presence of creep cavities and microcracks near the fracture frontier. The higher magnification micrograph confirms the presence of higher density of precipitates in the fracture frontier region (top right in Fig. 15, *a–b*). The EDS line scan of the fractured frontier confirms the presence of secondary phase carbide precipitates, as shown in Fig. 15, *c–d*.

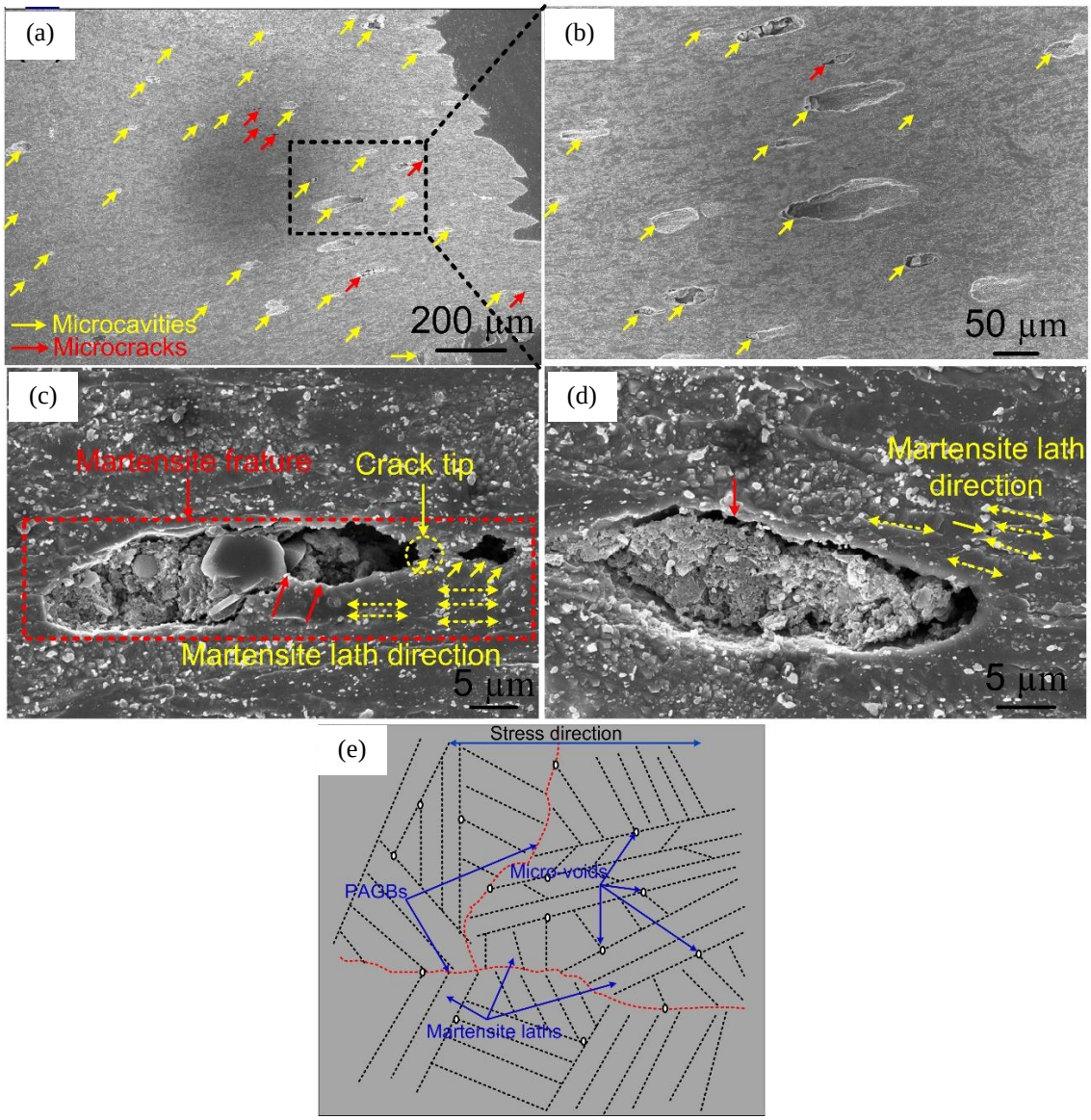

Fig. 14. Fracture frontier for PWNT 2 condition: (a) macroscopic view of cross-section, (b) elongation of creep cavities along loading direction (c) martensite fracture within martensite laths and martensite cracking along lath boundaries in direction of martensitic laths, (d) detailed view of microcavities, (e) the schematic of the creep voids located at the triple boundaries corresponding to the structure details as shown in Fig. 9, *a–d*, Fig. 10, *b*, Fig. 11, *c*, Fig. 12, *b* and Fig. 13, *c* and Fig. 14, *c*

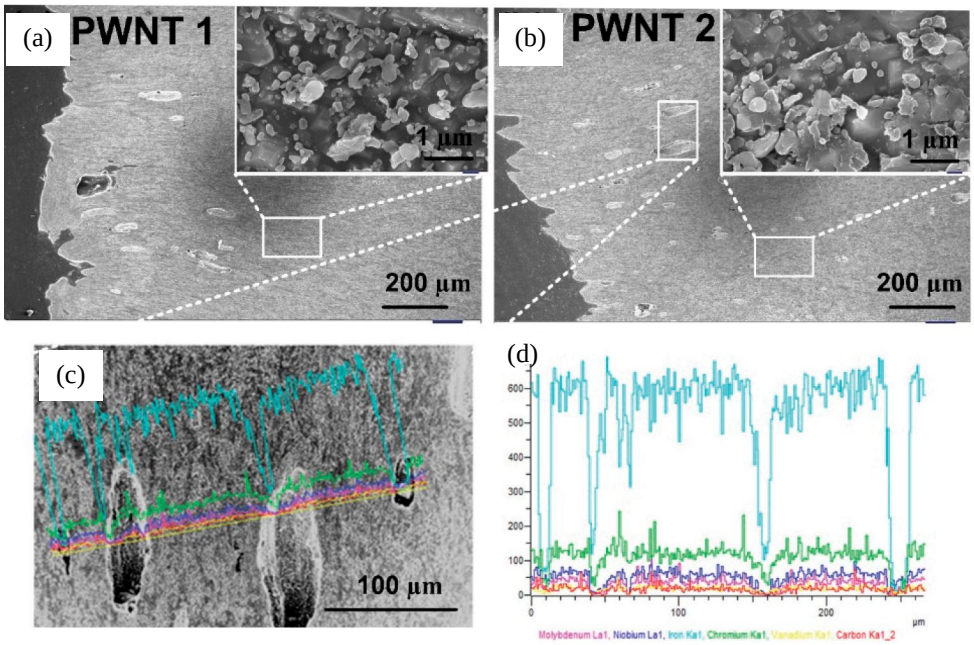

Fig. 15. Detailed view of fracture frontier for sample (a) PWNT 1, (b) PWNT 2;
EDS line scan along the creep cavities (c) and (d) microstructure evolution across the weldments

The microstructure of fine grain heat affected zone (FGHAZ) in different creep test condition is shown in Fig. 16. For as-welded 1 condition, microstructure consists of equiaxed laths with agglomeration of precipitates inside the matrix region and near to PAGBs. In PWHT 1 condition, lath blocks are easily traceable from the precipitates. The PAGBs with fine precipitates are clearly observed, as shown in Fig. 16, *b*. The precipitates observed in PWHT 1 condition are smaller in size as compared to as-welded 1 condition. In PWNT 1 condition, PAGBs are observed to be decorated with coarse precipitates. The laths blocks are also observed inside the PAGBs, as shown in Fig. 16, *c*. For as-welded 2 condition, i.e. low applied stress of 150 MPa, microstructure looks similar to as-welded 1 condition with the smaller size of precipitates, as shown in Fig. 16, *d*. In PWHT 2 condition, the size of precipitates is observed to be higher as compared to as-welded 2 condition. The equiaxed lath morphology is also observed, as shown in Fig. 16, *e*. The microstructure of PWNT 2 condition looks completely different due to the presence of many coarse precipitates along the boundaries. The Laves phase formation is also observed for PWNT 2 condition which is confirmed in later discussion. The Laves phases are generally observed along the lath boundaries and PAGBs, as shown in Fig. 16, *f*. The detailed phase analysis was carried out using the elemental and line mapping as discussed later.

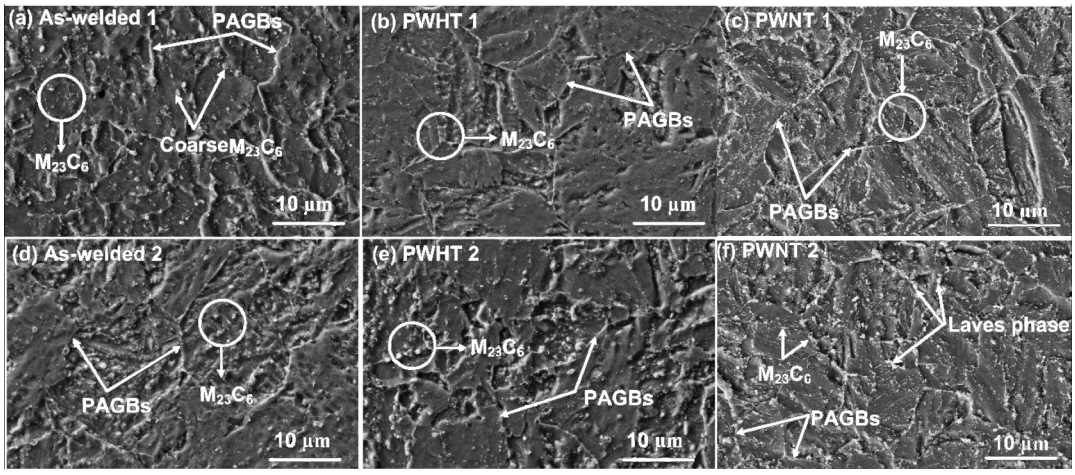

Fig. 16. Microstructure of fine-grained heat affected zone (a) as-welded 1, (b) PWHT 1,
(c) PWNT 1, (d) as-welded 2, (e) PWHT 2 and (f) PWNT 2

The detail microstructure analysis of weld fusion zone for the crept sample exposed at 620 ^{o}C for 200 MPa (as-welded 1) is shown in Fig. 17. The coarse precipitates are observed at the lower magnification, as shown in Fig. 17, *a*. At higher magnification, agglomeration of precipitates is observed, as shown in Fig. 17, *b*. A lot of fine $M_{23}C_6$ precipitates form a cluster and get collected around the single particles.The agglomeration of precipitates form in different size and morphology. The agglomeration is generally observed inside the matrix region. The precipitates along the lath and grain boundaries do not show such type of behaviour.

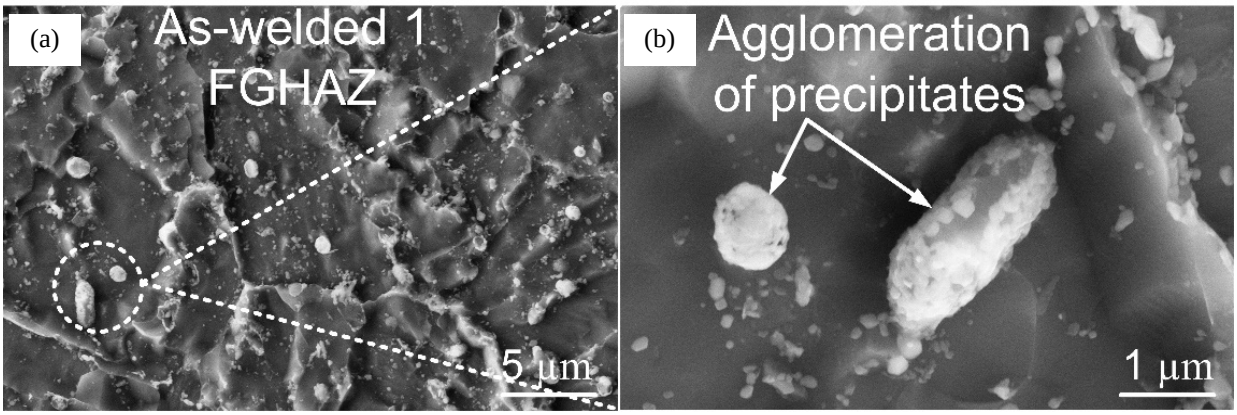

Fig. 17. Microstructure of weld fusion zone for creep exposure at 620 ^{o}C at stress of 200 MPa (as-welded 1 condition)

In as-welded and PWHT condition, microstructure looks similar in FGHAZ except for the lath morphology and agglomeration of precipitates in as-welded 1 condition. The coarse precipitates of size in the range of 300–400 nm are observed in PWNT 1 condition. The microstructure of various heat affected zone and weld fusion zone for the crept welded sample in PWNT 1 and PWNT 2 condition are shown in Fig. 18. For PWNT 1 condition, coarse bulky precipitates are observed in the weld fusion zone while in HAZs the precipitate morphology looks similar. In PWNT condition, the precipitates formed are generally bigger in size as compared to PWHT. The lath morphology is clearly observed in HAZs. For PWNT 1 condition, the size of the cluster in weld fusion zone is measured in the range of 370–1227 nm with an average of 820 nm. In HAZs, the size of $M_{23}C_6$ precipitates of spherical shape is measured in the range of 60–335 nm. The coarse precipitates are generally observed along the PAGBs. The needle-shaped particles having width varies from 68 to 127 nm with an average of 87±21 nm and length from 238 to 463 nm with an average of 327±78 nm. The precipitates having a size in the range of 20–35 nm are also observed inside the matrix region which is confirmed as Nb-rich MX precipitates from the later discussion. In weld fusion zone Fig. 18, *a*, the cluster formation might be due to the nucleation and coarsening of Laves phase. For PWNT 2, the microstructure of each zone is shown in Fig. 18, ***e–h.*** In PWNT 2 condition, the clustering of precipitates is observed along the PAGBs and lath boundaries in each zone which are confirmed as the Laves phase. Hence, In PWNT condition, longer creep exposure time leads to the formation of Laves phase in weld fusion zone and HAZs. The size of $M_{23}C_6$ precipitates is varied from the 90–285 nm. The precipitates observed in weld fusion zone and FGHAZ are generally globular or spherical shape. The needle-shaped particles are observed in FGHAZ and ICHAZ. The width of needle shape particles varies from 68 to 174 nm with an average of 113±34 nm and length from 208 to 404 nm with an average of 282±72 nm. The size of bulky clusters is measured in the range of 1132–1160 nm. The needle or chain-likeshape and bulky particles are confirmed as the Laves phase. The size of Nb and V-rich fine MX particles are measured in the range of 20–40 nm. Hence, In PWNT 2 condition, the presence of coarse precipitates after the heat treatment leads to the formation of Laves phase during the creep exposure. The detail characterization of the Laves and $M_{23}C_6$ phase is discussed in the next section.

In as-welded 2 and PWHT 2 condition, fracture occurs in soft FGHAZ. The elemental mapping of the precipitates in FGHAZ confirms the higher concentration of Cr with Mo and Nb, as shown in Fig. 19, *a*. The higher concentration of alloying elements like Cr and Mo on the precipitates leads tothe

formation of Cr and Mo-rich $M_{23}C_6$ precipitates while Nb concentration confirms the segregation of Nb-rich precipitates along the PAGBs. In as-received condition, microstructure generally consisted of Fe, Mo and Cr-rich $M_{23}C_6$ precipitates but during the creep exposure the Cr and Mo weight percentage was reported to be increased in $M_{23}C_6$ composition. The line mapping also confirmed the increase in weight percentage of Cr and Mo in $M_{23}C_6$, as shown in Fig. 19, *b–c*. The elemental mapping of PWHT 2 condition is also carried out in FGHAZ which confirm the formation of Mo and Cr-rich $M_{23}C_6$ precipitates, as shown in Fig. 19, *d*.There is no any evidence is observed for the Laves phase.

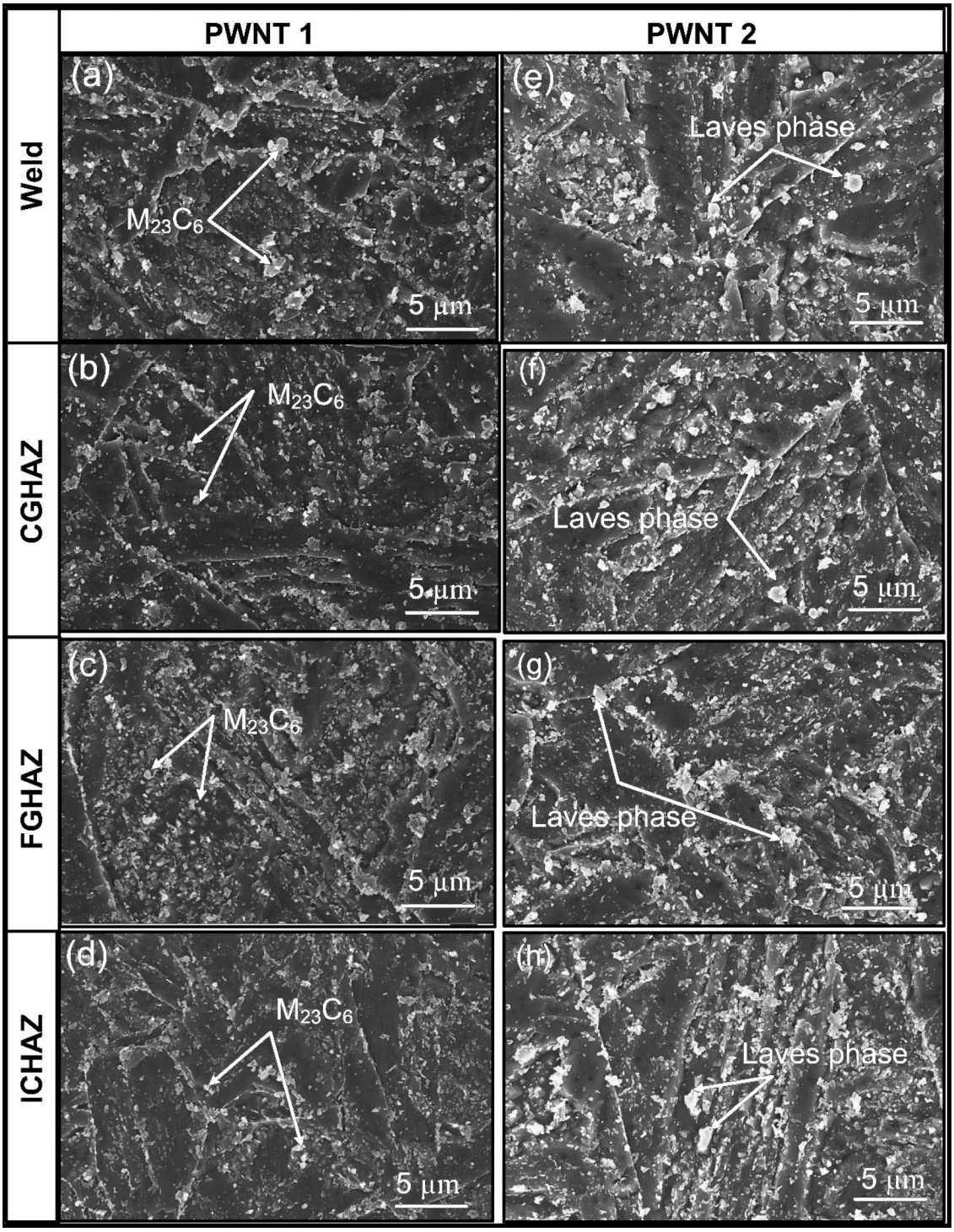

Fig. 18. Microstructure of subzones in PWNT 1 and PWNT 2 condition (a) and (e) weld fusion zone; (b) and (f) CGHAZ; (c) and (g) FGHAZ; (d) and (h) ICHAZ

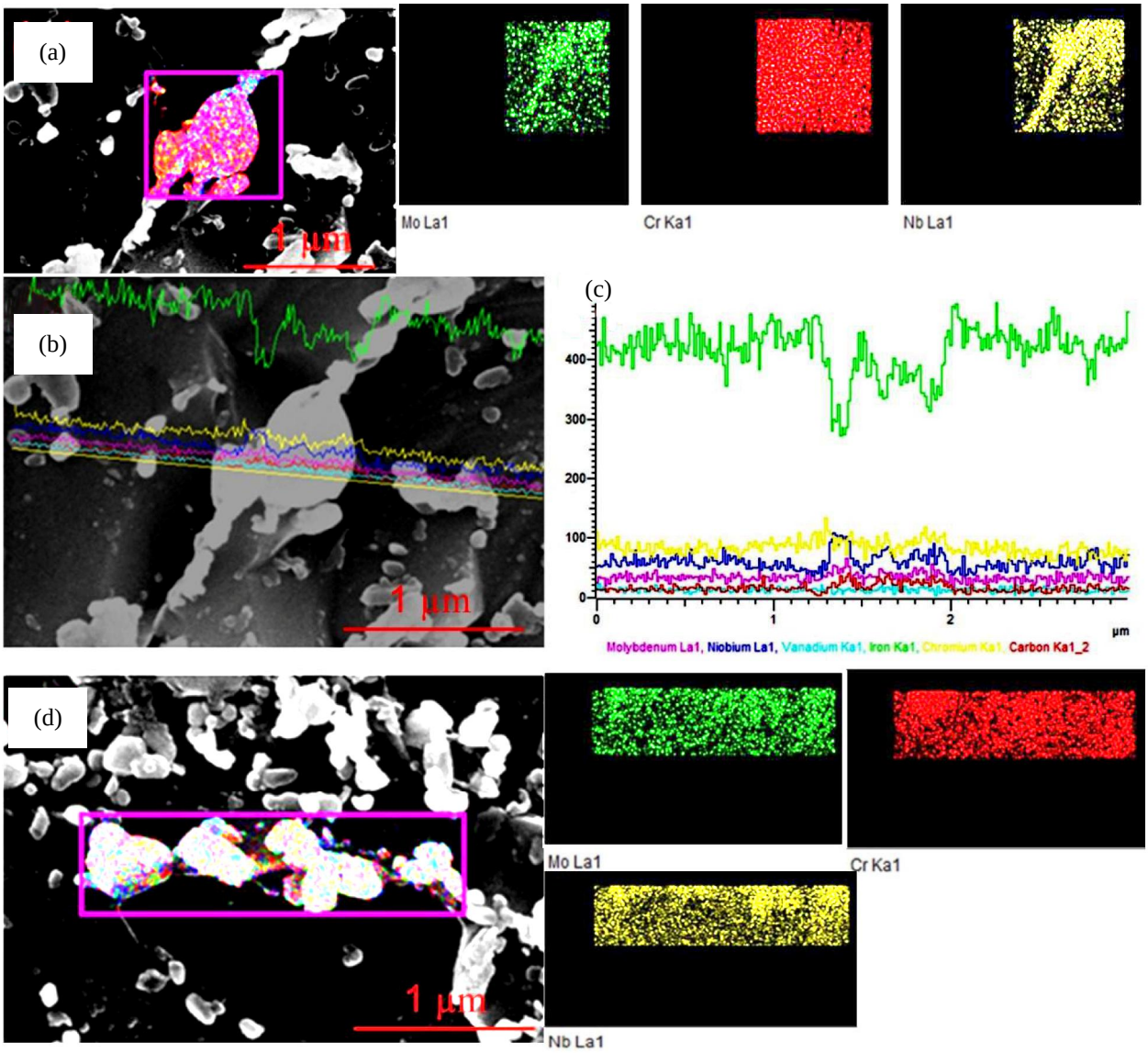

Fig. 19. (a) Elemental mapping of the FGHAZ for as-welded 2 conditions (150 MPa/620 ^{o}C), (b) and (c) line mapping of the precipitates; (d) elemental mapping of the FGHAZ for PWHT 2 condition (150 MPa/620 ^{o}C)

For PWNT 1 condition, the fracture zone and the EDS spectra of the precipitates are shown in Fig. 20, *a*, *b*, respectively. In PWNT 1 condition, fracture frontier exists in the base zone. The EDS spectra confirm the higher weight percentage of Cr, Fe and Mo along with Nb. The higher weight percentage of the Cr, Fe and Mo ensure the formation of $M_{23}C_6$ precipitates while Nb confirms the formation of Nb-rich MX precipitates. The EDS spectra also show the composition of the Fe-matrix. The line mapping of the precipitates also confirms the increase in weight percentage of Cr in $M_{23}C_6$ after the creep exposure, as shown in Fig. 20, *c–d*. The elemental mapping confirms the higher weight percentage of Cr and Nb in Fe-matrix. The Mois generally observed along the PAGBs and shows the heterogeneous distribution inside the Fe-matrix. The Cr particle density is observed to be higher along the PAGBs, i.e. in $M_{23}C_6$ while lower in matrix region. The Fe distribution shows the opposite result of Cr. The distribution of alloying elements on the precipitates confirms the formation of Cr and Mo-rich $M_{23}C_6$ phase with higher weight percentage of Cr.

The EDS spectra of the precipitates form in the different zone of the crept PWNT 1 sample is given in Table 5. The points selected for the EDS spectra are given in Fig. 21.

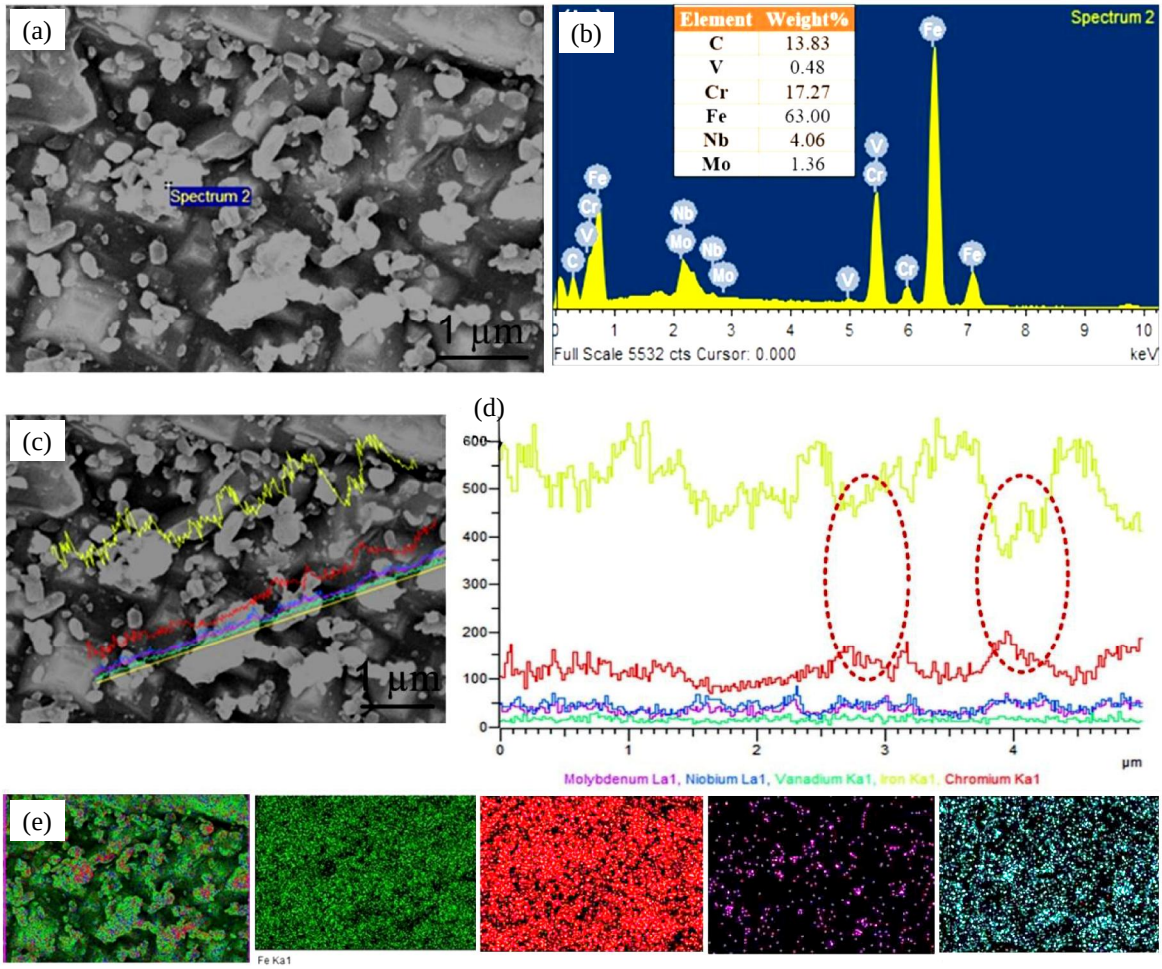

Fig. 20. (a) Microstructure of the fracture frontier for PWNT 1 condition (200 MPa/620 ^{o}C), (b) EDS spectra of the spectrum 2; (c) and (d) line mapping of the precipitates; (e) elemental mapping of the fracture frontier

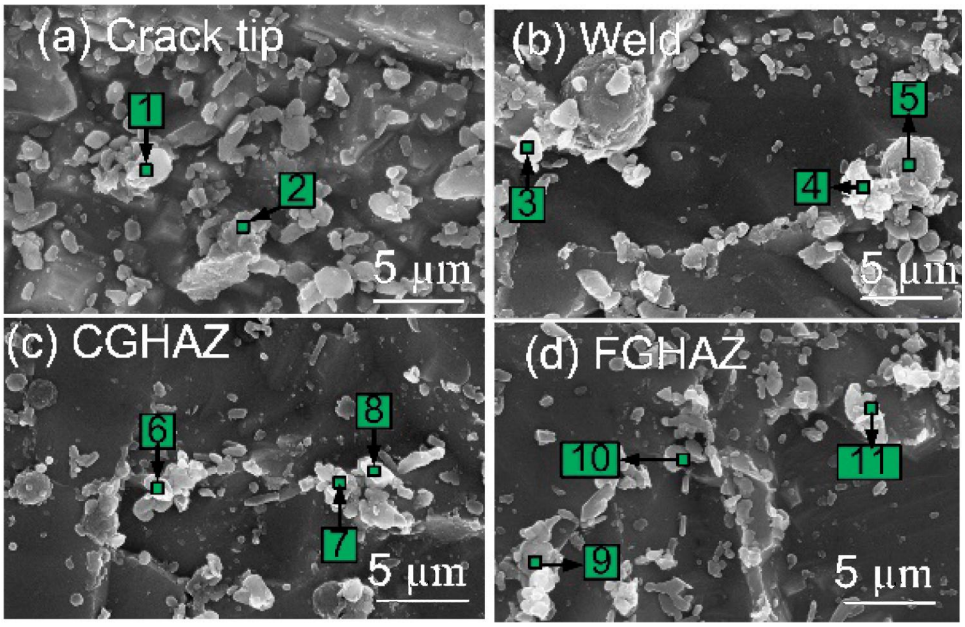

Fig. 21. Microstructure of subzones in PWNT 1 condition used for the EDS spectra, (a) crack tip, (b) weld fusion zone, (c) CGHAZ, (d) FGHAZ

Table 5

The EDS spectra of the point shown in Fig. 21.

Point No.	EDX results of precipitates; element wt. %						
	C	Cr	Fe	Mo	V	Nb	Possible Phase
1	13.83	17.27	63.00	1.36	0.48	4.06	Cr-Mo-rich $M_{23}C_6$
2	12.80	19.30	62.06	1.36	0.30	4.18	Cr-Mo-rich $M_{23}C_6$
3	7.45	19.76	61.97	–	0.56	10.26	Cr-rich $M_{23}C_6$, Nb-rich NbX
4	10.30	11.22	60.47	11.02	0.35	6.95	Mo-rich Laves phase, Nb-rich NbX
5	10.76	13.45	58.62	11.38	1.83	13.95	Mo-rich Laves phase, Nb-rich NbX
6	19.10	15.97	55.21	–	0.45	9.26	Cr-rich $M_{23}C_6$, Nb-rich NbX
7	16.28	14.17	59.19	3.17	0.34	6.85	Cr-Mo-rich $M_{23}C_6$, Nb-rich NbX
8	12.05	16.28	64.44	0.89	0.42	5.92	Cr-rich $M_{23}C_6$, Nb-rich NbX
9	13.80	12.89	64.80	–	0.83	7.67	Cr-rich $M_{23}C_6$, Nb-rich NbX
10	11.83	16.58	60.97	–	1.00	9.62	Cr-rich $M_{23}C_6$, Nb-rich NbX
11	15.50	15.68	59.64	–	0.75	8.43	Cr-rich $M_{23}C_6$, Nb-rich NbX

The EDS spectra of the precipitates near the crack tip confirm the formation of Cr and Mo-rich $M_{23}C_6$ precipitates. The higher weight percentage of Nb shows the formation of Nb-rich MX particles. In weld fusion zone, the EDS spectra of point 3 confirm the formation of Cr and Mo-rich $M_{23}C_6$ and Nb-rich MX precipitates while the EDS spectra of point 4 and 5 shows the formation of Mo-rich Laves phase and Nb-rich NbX precipitates. In another zone, the EDS spectra show the similar results and confirm the formation of Cr-rich $M_{23}C_6$ and Nb-rich MX precipitates. For detail investigation of the Laves phase formation in weld fusion zone, line and elemental mapping are performed, as shown in Fig. 22.

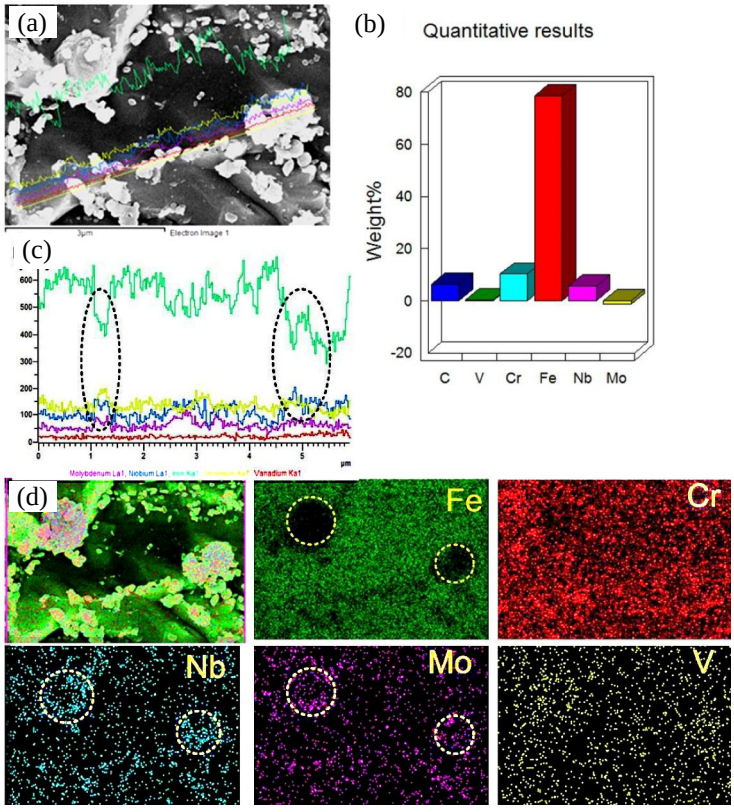

Fig. 22. For PWNT 1 condition: (a) micrograph of weld fusion zone at 50 Kx, (b) EDS spectra of the matrix, (c) line mapping of the precipitates, (d) elemental mapping of the precipitates

For PWHT 2 and as-welded 2 conditions, fracture occurred from the soft FGHAZ which are characterized in Fig. 19 and no any evidence of Laves phase formation is observed. In PWNT 1 condition, fracture occurs from the base zone which is characterized in Fig. 20. The elemental and line mapping confirm the formation of coarse $M_{23}C_6$ precipitates while in weld fusion zone of the PWNT 1 sample, the Laves phase formation is confirmed by Table 5. The elements Fe, Cr, Mo and Nb show the heterogeneous distribution in as-received condition as well as in fracture frontier zone of PWNT 1 condition as shown in Fig. 20. After the creep exposure, the accumulation of Mo and Nb took place in some specific region, as shown in Fig. 22, *d*. The Mo-rich regions related to the formation of Laves phase and Nb-rich region can be considered as the accumulation of fine NbX precipitates. The Mo-rich region seems to be surrounded by Cr-rich precipitates. Fig. 22, *a* shows the morphology and clustering behaviour of the Laves phase. The size of Laves phase is observed to be higher than the $M_{23}C_6$ precipitates as a result of their fast growing nature. The mean size of Laves phase is measured to be 350 nm. The line mapping of the cluster of precipitates also confirms the higher intensity of Mo and Nb peaks, as shown in Fig. 22, *c*. That results in formation of NbX and Laves phase. The EDS spectra of the matrix are shown in Fig. 22, *b*.

In PWNT 2 condition, each zone shows the accumulation of the coarse precipitates along the PAGBs after the creep rupture, which is depicted in Fig. 23, *e–h*. The clustering behaviour of the precipitates along the PAGBs shows the formation of the Laves phase. In order to confirm the formation of the Laves phase, the different zone of the crept PWNT 2 sample is characterized using the line and elemental mapping. The weld fusion zone characterization is shown in Fig. 23. Fig. 23, *a* shows the agglomeration of the precipitates. The EDS spectra of the precipitates as shown in Fig. 23, *b* confirms the higher weight percentage of Mo, Cr andNb that leads to the formation of Mo and Cr-rich $M_{23}C_6$, Mo-rich Laves phase and Nb-rich MX precipitates. The line mapping shows the drastic decrease in the peak intensity of Fe at the precipitates and same time drastic increase in peak intensity of Mo and Nb, as shown in Fig. 23, *c–d*. The higher peak intensity of Mo and Nb alloying elements also confirm the formation of Laves phase in the weld fusion zone. The elemental mapping of the weld fusion zone is shown in Fig. 24. The elemental mapping of the precipitates shows the uneven distribution of the precipitates like Mo, Cr, Fe and Nb. The accumulation of Nb and Mo elements and diminishing of Fe particles at the coarse precipitates confirm the Laves phase formation along with fine NbX precipitates. The ellipsoidal particles having ahigher density of Mo and depleted in Fe and Cr should be considered as Mo-rich Laves phase as shown in Fig. 23, *a*. The density of Fe elements in the Laves phase is observed to be lower as compared to the martensite matrix phase. The Mo-rich Laves phase and Nb-rich NbX precipitates are mainly surrounded by the Cr-rich $M_{23}C_6$ precipitates.

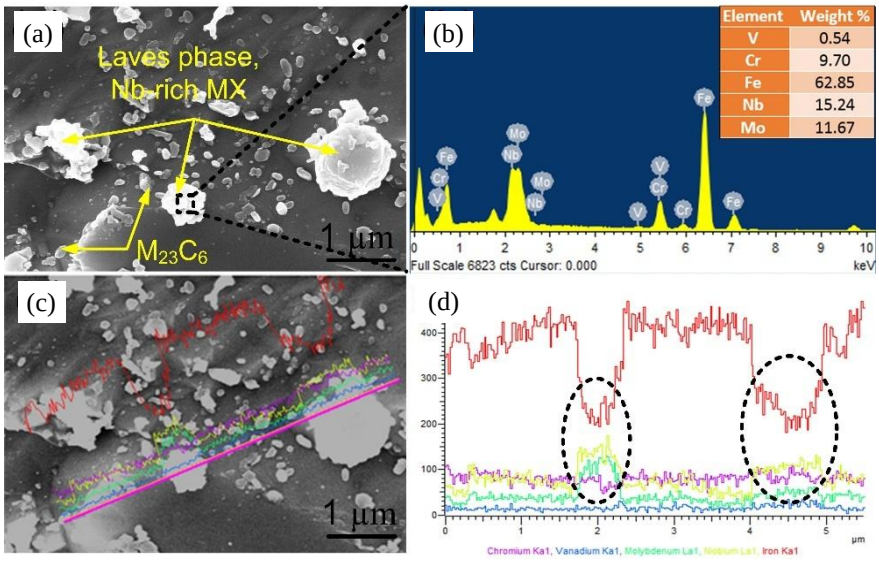

Fig. 23. (a) Microstructure of weld fusion zone in PWNT 2 condition used for EDS spectra, line mapping and elemental mapping, (b) EDS spectra of particle, (c) and (d) line mapping

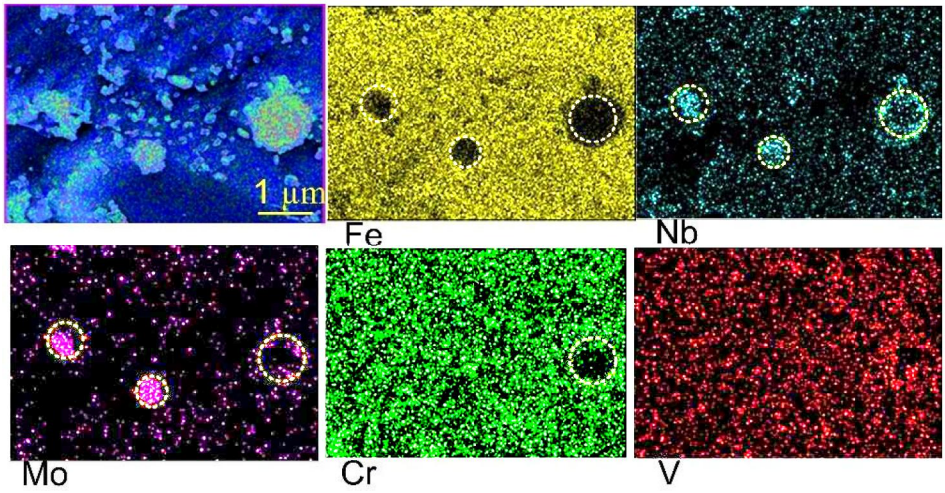

Fig. 24. Elemental mapping of the weld fusion zone of crept sample in PWNT 2 condition

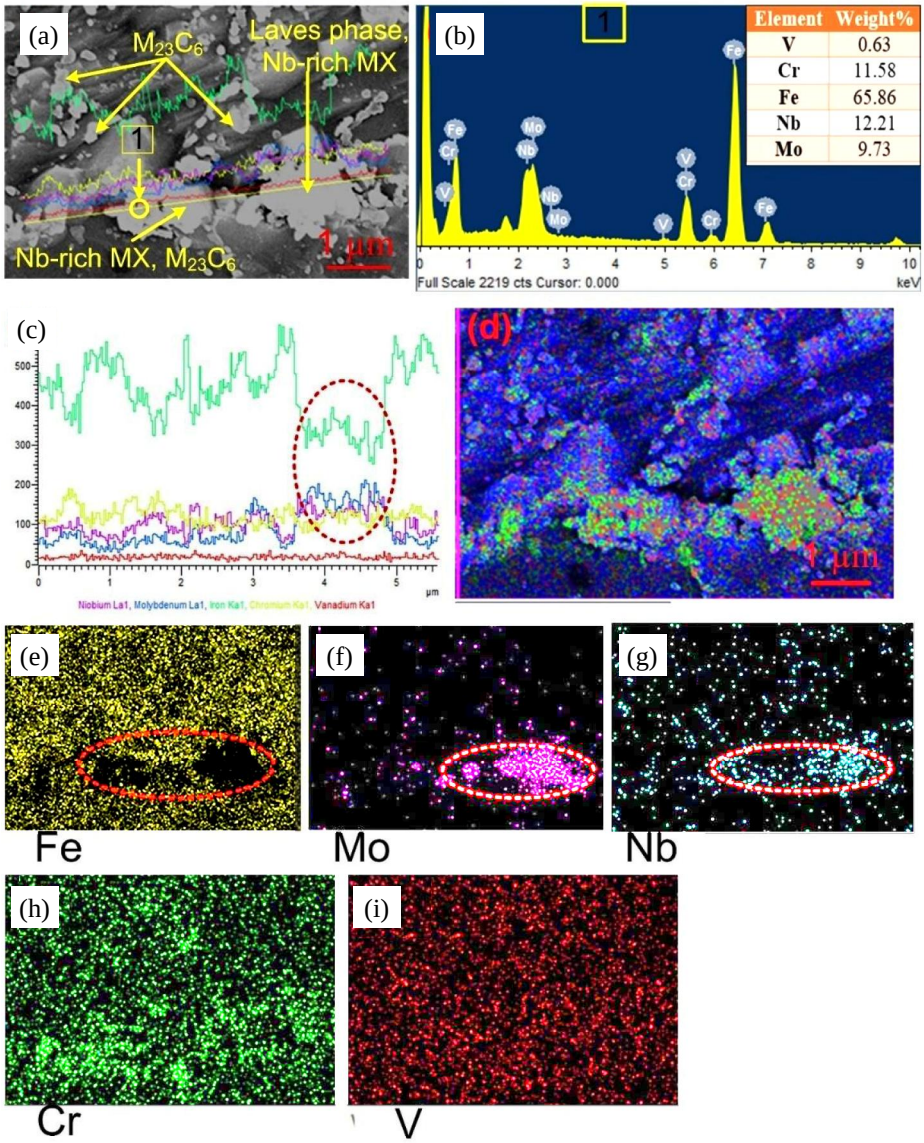

Fig. 25. (a) Microstructure of FGHAZ in PWNT 2 condition used for EDS spectra, line mapping and elemental mapping, (b) EDS spectra of particle, (c) line mapping; elemental mapping (d) combine elemental mapping, (e) Fe, (f) Nb, (g) Mo, (h) Cr, (i) V

For PWNT 2 condition, characterization of FGHAZ in thecrept sample is shown in Fig. 25. The microstructure used in elemental analysis and line mapping is shown in Fig. 25, *a*. The EDS spectra confirm the higher weight percentage of Mo, N band Cr which indicate the formation of Laves phase, Mo and Cr-rich $M_{23}C_6$ and Nb-rich NbX. The EDS spectra are shown in Fig. 25, *b*. The line mapping of the precipitates also shows the higher peak intensity of Mo and Nb at coarse precipitates and higher peak intensity of Cr at point 1. The combined elemental mapping is shown in Fig. 25, *d*. The bulk depositions of Mo and Nb at bigger size precipitates confirm it as Laves phases along with NbX, as shown in Fig. 25, *f–g*. Fig. 25, *d* shows the higher concentration of Cr around the bigger size particles or Laves phase. However, no change in thedistribution of V is observed, as shown in Fig. 25, *i*.

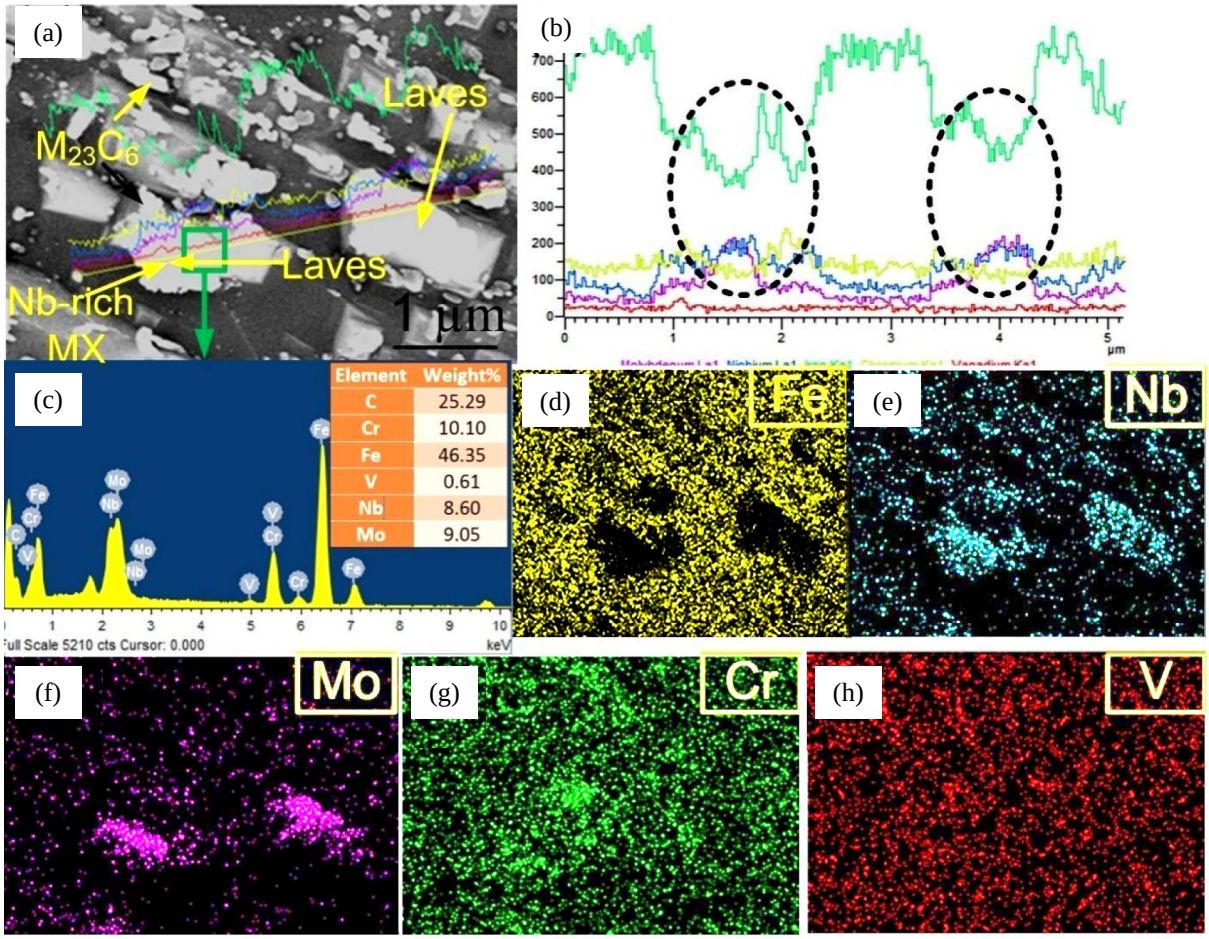

Fig. 26. (a) Microstructure of ICHAZ in PWNT 2 condition used for EDS spectra, line mapping and elemental mapping, (b) line mapping, (c) EDS spectra of particle; elemental mapping (d) Fe, (e) Nb, (f) Mo, (g) Cr, (h) V

In PWNT 2 condition, inter-critical heat affected zone (ICHAZ) of the crept sample is shown in Fig. 26, *a* at 50000x magnification. The EDS spectra of the bulky precipitate are shown in Fig. 26, *c* that ensure the formation of Laves phase and Nb-rich MX precipitates. The line mapping also shows the drastic increase in the peak intensity of the Mo and Nb at the precipitates with asimultaneous decrease in the peak intensity of Fe. However, a minute change is observed in the peak intensity of Cr. The elemental mapping of the bulky precipitates shows the higher density of Mo and Nb, as shown in Fig. 26, *e, f*, respectively. However, the Fe density is negligible at the bulky precipitates and it confirms the lower concentration of Fe in Laves phase as compared to the martensite matrix phase. The accumulation of Mo precipitate confirms the Laves phase formation in ICHAZ. In ICHAZ zone, Laves phase shows the chain like shape with bulky particles. Isik et al. [27] had reported the two stages of the Laves phase growth. At the initial stage of the nucleation, it grows into rod-like shape along the PAGBs and lath boundaries and after that it

morphs into chain-like shape and some bulky shape particles. In weld fusion zone, the Laves phase is observed in bulky shape while in the ICHAZ, the chain-like shape is observed.

The evolution of Laves phase strongly affects the microstructure and creep behaviour of the P91 steel [24]. In P91 steel, Laves phase evolution is considered as harmful because the nucleation and growth of Laves phase result in diffusion of Mo from thematrix to Laves phase and leads to weakened solution strengthening [30]. In PWNT 2 crept sample, the clustering nature of the Laves phase results in lath widening due to areduction in preventing theeffect of Laves phase to lath boundaries migration. In P92 steel, strengthening from the Mo atoms is considered at theimportant strengthening mechanism. However, the precipitation of intermetallic Laves phase is inevitable for P92 steel because Mo and W are the main alloying element in Laves phase. Zhang et al. [31] had concluded that the formation of Laves phase is thought to be responsible for premature failure during the creep exposure as a result of void growth.

The nucleation and growth of the Laves phase is also summarized in a schematic microstructure scenario, as shown in Fig. 27. Fig. 27, *a* shows the preferential sites for $M_{23}C_6$ nucleation (micrograin boundary).The precursor phenomenon of the Laves phase nucleation during the creep exposure is shown in Fig. 27, *b*. It shows the segregation of Mo particles along the micrograin boundary. The nucleation of Laves phase particle at micrograin boundary is shown in Fig. 27, c shows. It generally nucleates at the $M_{23}C_6$ particles. After the nucleation, it acquires the bulky shape as a result of fast growth rate, as shown in Fig. 27, *d*. The elemental mapping clearly shows the segregation of Mo to internal interfaces. The growth of Laves phase also results in swallowing of the $M_{23}C_6$ and other useful particles that results in the reduction of creep rupture strength.

The volume fraction of the Laves phase has a great effect on the strengthening mechanism as presented in Fig. 28. On one hand, the evolution of Laves phase results in loss of solid solution strengthening due to consumption of Mo from the solution matrix. On another hand, the precipitation strengthening the effect of Laves phase depends on both the volume fraction of the precipitates and means size of the Laves phase. The combined effect of the volume fraction of the Laves phase and their size is shown in curve 1.

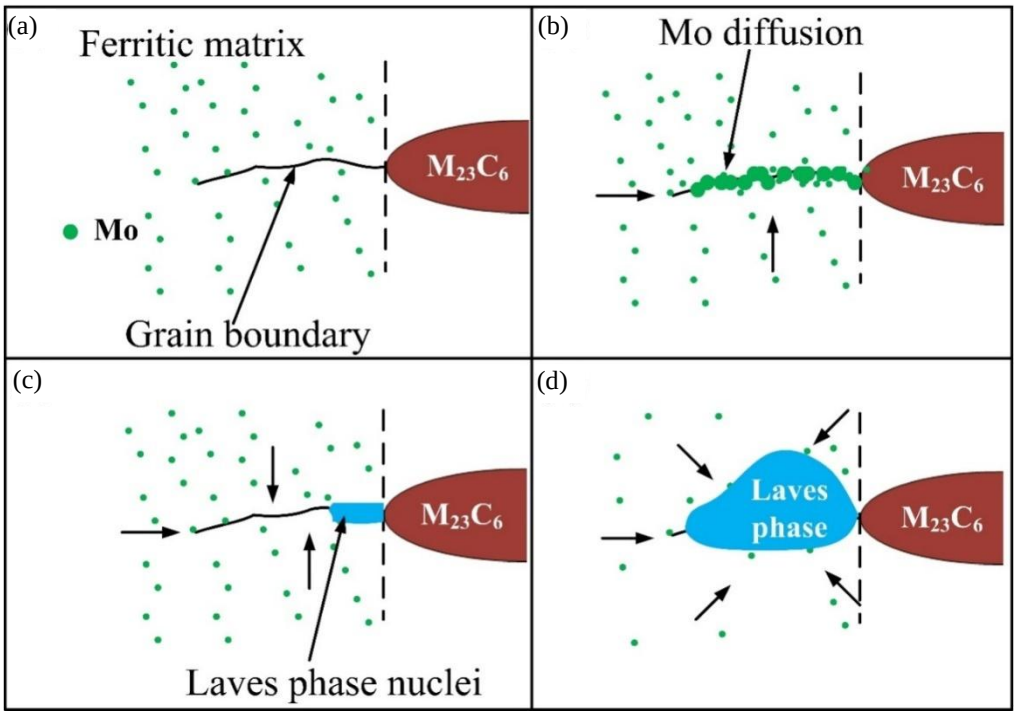

Fig. 27. Different stages of Laves phase nucleation, (a) as-received microstructure, (b) segregation of Mo particles along the subgrain boundary during creep exposure, (c) nucleation and rod-like growth of Laves phase in direction of subgrain boundary and (d) bulky shape Laves phase in the last stage

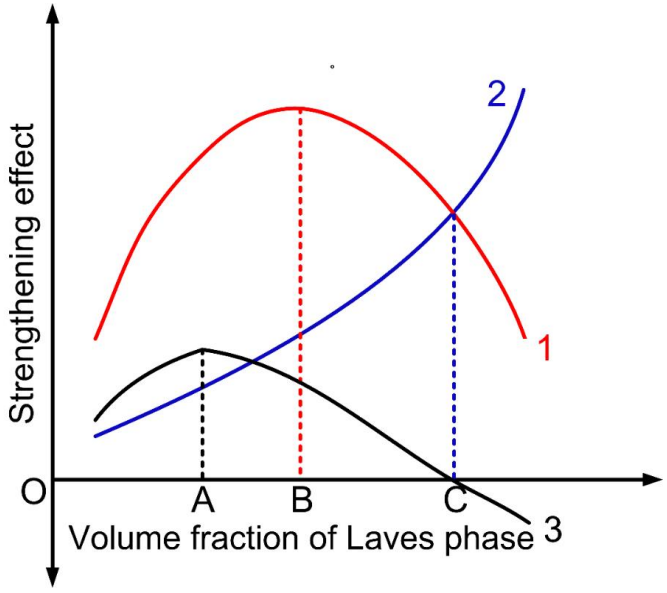

Fig. 28. Schematic diagram showing the relationship between creep rupture strength and volume fraction of Laves phase. Curve 1: Laves phase formation and increase in creep rupture strength for precipitation strengthening; Curve 2: decrease in creep rupture strength for loss in solution strengthening caused by reduction in amount of solute atoms Mo; Curve 3: combined effect of curve 1 and curve 2

At the initial stage of the precipitation, fine Laves phase provides effective pinning effect to subgrain boundaries upto point B but at the second stage due to higher coarsening rate precipitation strengthening effect from Laves phase began to decline. The formation of Laves phase also consumes the $M_{23}C_6$ precipitates by nucleating on it and swallowing to it. The combined effect of precipitation strengthening and solid solution strengthening is shown in curve 3. It concludes that creep rupture strength might be enhanced at the initial stage of fine Laves phase formation and after that it drops due to thehigher growth rate of the Laves phase.

Fracture mechanism analysis

To understand the fracture behaviour of the crept P92 welded specimen in different operating conditions, the morphology of the fracture surfaces were studied using the SEM images. Fig. 29 shows the top view of the fracture surface and detailed view of the fiber zone of creep ruptured specimen in as-welded, PWHT and PWNT condition for creep exposure temperature of 620 ^{o}C and applied stress of 200 MPa. Fig. 29, *a* shows the top view of the fracture surface of creep ruptured specimen in as-welded 1 condition, exhibiting the ductile cup like features. The fracture surface reveals the shear lip zone at the outer periphery and a fiber zone at the central region. In the outer periphery, flat surfaces are observed in the shear-lop zone that consists of the shear dimples as a result of shear stress. In the fiber zone, both deep and equiaxed fine dimples are observed that confirms the dimple rupture leads to the ductile fracture under creep exposure condition, as shown in Fig. 29, *b*. For PWHT 1 condition, the top view and detailed view of the fiber zone is shown in Fig. 29, *c*, *d*, respectively. The top view shows the significant necking behaviour and the shear lip zone is also observed to be reduced as compared to as-welded 1 condition. The fiber zone shows the dense packing of the non-uniform ductile dimples, as shown in Fig. 29, *d*. In PWNT 1 condition, the shear-lip zone is observed to be missing, as shown in Fig. 29, *e*. The equiaxed dimples are still remained in the fiber zone and confirm the ductile fracturing. The fracture morphology suggests that in case of short-term creep deformation under the tested conditions, ductile fracturing is the dominant fracture

mechanism. In case of as-welded 1 and PWHT 1 condition, fracture surface reveals the shear-lip zone. But for PWNT 1 condition, the shear-lip zone remains absent. The detailed view of the fiber zone clearly confirms the transgranular mode of the fracture in all the creep test conditions. However, the number density of fine dimples, deep dimples and their size are observed to be varied for different creep test conditions.

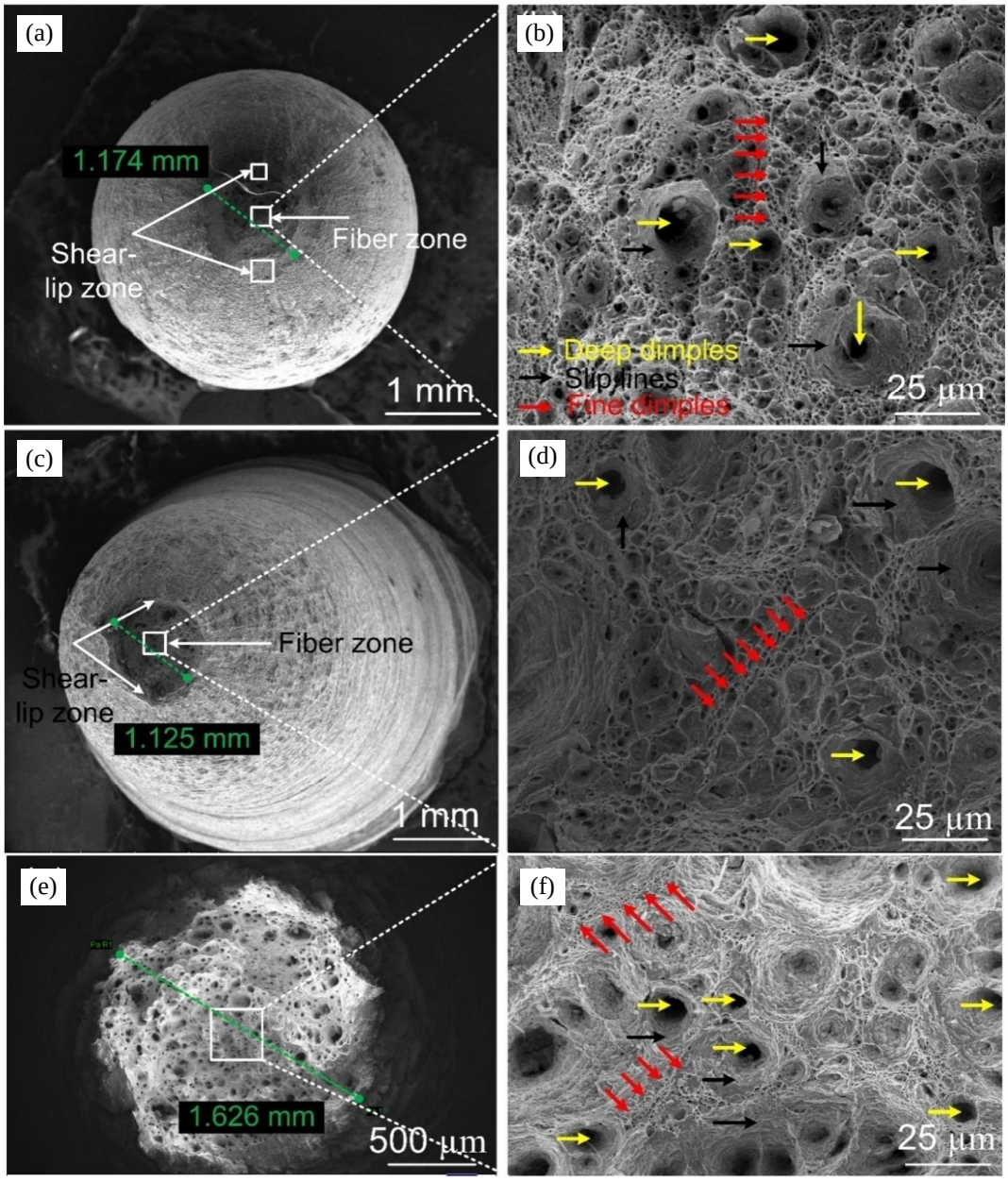

Fig. 29. SEM fracture surface images of ruptured specimen at 620 °C under 200 MPa;
for as-welded condition (a) macro view (b) magnified view of the fiber zone showing equiaxed dimples;
for PWHT condition (c) macro view (d) magnified view of the fiber zone showing equiaxed dimples;
for PWNT condition (e) macro view (f) magnified view of the fiber zone showing equiaxed dimples

The number of fine dimples is observed to be more for a high level of the applied stress for both PWHT and PWNT condition. The slip lines observed in fiber zone are associated with the large plastic deformation.From the higher magnification micrograph of the fiber zone, both fine and deep dimples are observed at the fracture surface. The density of deep dimples is observed to be higher for as-welded 1 and

PWNT 1 condition. Fig. 30, *d, f* shows the few regions of fine dimples present between the deep dimples. The deep dimples areas may be associated with the precipitates. Both $M_{23}C_6$ and Laves phase are brittle by nature as compared to the matrix that results in deformation gradient between precipitates and matrix under creep exposure condition. Hence, the precipitates can accelerate damage by providing the sites for the crack nucleation. These precipitates are generally associated with the grain and lath boundaries and some brittle intergranular fracture might be associated with the samples tested at the lower stress. The deep dimples are formed as a result of stress concentration at the coarse Laves phase and $M_{23}C_6$ phase. The increase in localized stress at the matrix-particle interface leads to excessive plastic deformation that results in the formation of micro-cracks.

The SEM fractographs of the crept sample for the low applied stress of 150 MPa in PWHT and PWNT conditions are shown in Fig. 30. Shear-lip zones are observed in PWHT condition while remaining absent in PWNT condition.

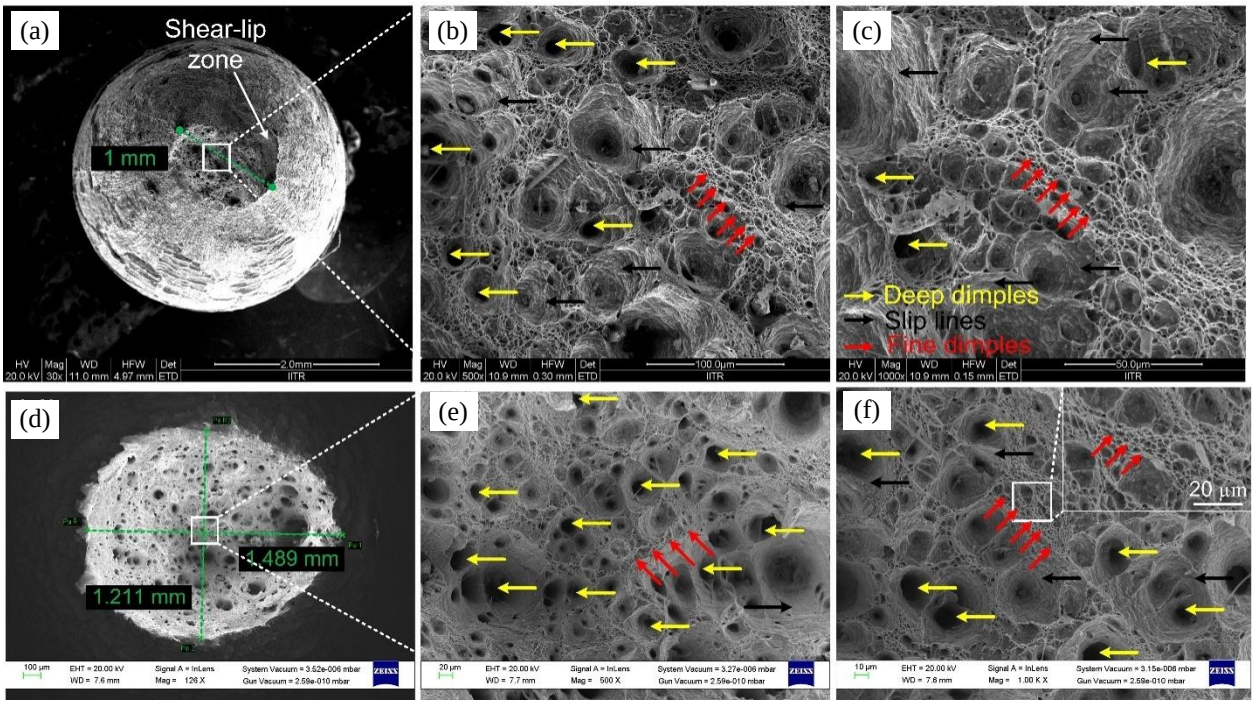

Fig. 30. SEM fracture surface images of ruptured specimen at 620 °C under 150 MPa; PWHT condition (a) macro view (b) magnified view of the fiber (c) magnified view at 1000x showing deep dimples, fine dimples and slip lines; for PWNT condition (d) macro view (e) magnified view of the fiber zone showing equiaxed dimples (f) magnified view at 1000x showing deep dimples, fine dimples and slip lines

The density of fine dimples and deep dimples are observed to be increased in case of low level of applied stress for both PWHT and PWNT condition, as shown in Fig. 30, *b*, *e*, respectively. The size of deep dimples is also observed to be increased in case of low level of applied stress. The fine dimples are observed besides the area of deep dimples, as shown in higher magnification fractographs (Fig. 30, *c–f*). As compared to low applied stress (150 MPa), the shear lip phenomena is more dominant in high applied stress (200 MPa) for both PWHT 1 and PWNT 1 condition, as shown in Fig. 30, *a*, *c*, respectively. In high-stress regimes (as-welded 1 and PWHT 1), propagation of crack by void sheet mechanism leads to the shear lip zone formation wherein the stress concentration at the ends of the small crack initiated during creep induces shear bands at the ends. The higher strain concentration leads to the voids nucleation inside the shear bands. The splitting of void-sheet as the crack advances and leads to the formation of the shear-lip zone. The absence of the shear-lip zone for the low level of applied stress may be attributed to the fact

that fracture in such cases generally results from the microstructural evolution like the formation of intermetallic Laves phases, coarsening of $M_{23}C_6$ and widening of laths.

The Mo-rich Laves phase generally nucleates at the $M_{23}C_6$particles along the sub-grain boundaries having chain-like or rod-like shape. At the initial stage of grow, it grows into a rod-like shape which finally transferred into chain-like shape, and a few bulky shape particles, as shown in Fig . The schematic growth of Laves phase is shown in Fig. 31.

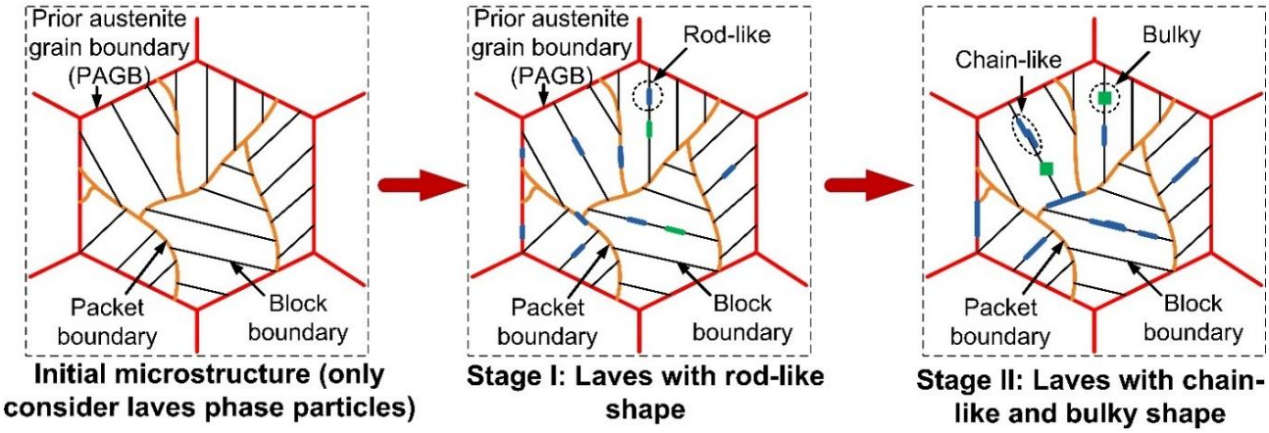

Fig. 31. Schematic growth of Lavesphase

Hardness before and after creep exposure

The variation in hardness for as-welded, PWHT and PWNT condition before the creep exposure are depicted in Fig. 32, *a–c*. A great variation in hardness was observed in as-welded condition. However, the heterogeneity gets reduced in PWHT condition. In PWNT condition, a negligible hardness variation was observed. After the creep exposure, in as-welded condition 1, fracture occurred in the base zone however in as-welded 2 condition fracture occurred in the FGHAZ. For low-stress regime, the hardness was measured to be much lower than the as-welded material. In as-welded 1 and as-welded 2 conditions, hardness near the crack tip was measured 179 HV (base zone) and 182 HV (FGHAZ). The average hardness of the weld fusion zone was measured to be 307 and 293 HV for as-welded 1 and as-welded 2 conditions, respectively. As compared to as-welded condition before creep tests, a drastic decrease in hardness (436 HV) was noticed after the creep tests. In PWHT condition, variation n hardness after the creep fracture is given in Fig. 32, *b*. In both the cases, fracture occurred in the FGHAZ (Type IV). The hardness near the crack tip was measured 192 and 177 HV for PWNT 1 and PWNT 2 condition.

The average hardness of the weld fusion zone was measured to be 224 and 222 HV for as-welded 1 and as-welded 2 condition, respectively which was much lower than the average hardness of weld fusion zone before the creep test (236 HV). However, a great variation in hardness was observed for the low-stress regime of 150 MPa (PWNT 2), as shown in Fig. 32, *b*. The variation in hardness for PWNT crept sample is shown in Fig. 31, *c*. For PWNT condition, the hardness was reported to be similar in each zone of the weldments. The hardness measured for the PWNT 1 condition was almost similar to PWNT before creep. However, a great reduction in hardness was noticed for the PWNT sample exposed at 620 ^{o}C for 150 MPa. The variation in hardness might be due to softening theeffect, grain coarsening and precipitate coarsening. For Both the PWNT crept sample, the fracture was noticed in the base zone as a result of homogeneity across the weldments. The hardness measured in the HAZ zone were 208 HV and 193 HV, respectively for PWNT 1 and PWNT 2 condition. However, the average hardness of weld fusion zone was measured to be similar for both creep condition and it was 203 HV.

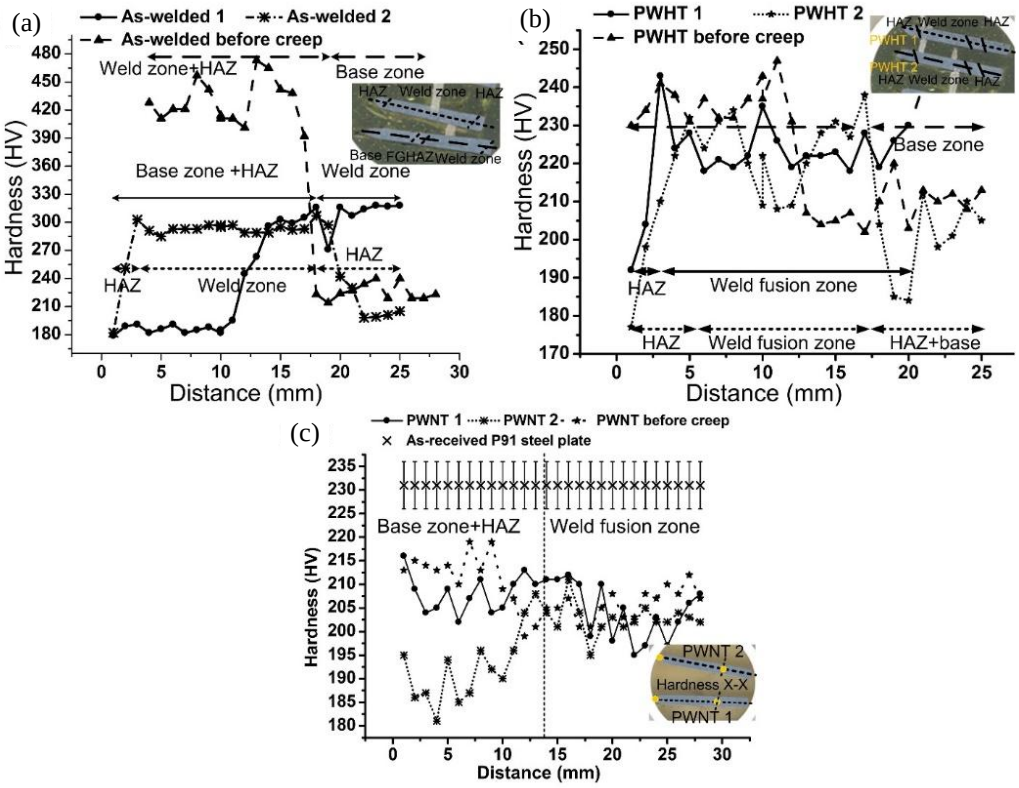

Fig. 32. Hardness variation for crept specimen with sites of Vickers hardness measurement
(a) For as-welded crept specimen, (b) for PWHT crept specimen, (c) for crept PWNT specimen

Conclusions

1. The PWNT treatment performed uniform hardness and microstructure along the transverse direction of welded joints. Creep tests were performed as welded, PWHT and PWNT conditions.

2. The creep tests of P92 steel performed at temperature of 620 ^{o}C in stress range of 150–200 MPa. Creep rupture life PWNT 2 condition 620 ^{o}C/150 MPa was measured 594.9 % higher than PWHT 2 condition and 142.8 % higher than as-welded 2 conditions.

3. Type IV fracture were measured as-welded 620 ^{o}C/150 MPa. The PWNT fracture occurred from base zone.

4. In PWNT condition, long-term creep exposure fracture occurs in the base zone as much away from the FGHAZ as a result of homogenization of microstructure. For a high level of applied stress at 200 MPa at 620 ^{o}C (PWNT 1), the microstructure of fracture frontier zone. In PWNT 2 condition, leaves phase formation was also observed at the fracture frontier zone.

5. The higher magnification micrograph of the fiber zone, both fine and deep dimples are observed at the fracture surface. The density of deep dimples is observed to be higher for as-welded 1 and PWNT 1 condition.

References

[1] R. B. Brucker, W. M. Elger, M. J. Sorek, M. S. Group, M. Engineer-, R. B. Brucker, W. M. Elger, Microstructure-thermal history correlations for HY-130 thick section weldments, *Weld*. J. 63 (1984) 254–262.

[2] K. Laha, K. S. Chandravathi, P. Parameswaran, K. B. S. Rao, S. L. Mannan, Characterization of microstructures across the heat-affected zone of the modified 9Cr-1Mo weld joint to understand its role in promoting type IV cracking, *Metall. Mater. Trans.* A. 38 (2007) 58–68. https://doi.org/10.1007/s11661-006-9050-0.

[3] Y. Tsuchida, K. Okamoto, Y. Tokunaga, Study of creep rupture strength in heat affected zone of 9Cr-1Mo-V-Nb-N steel by welding thermal cycle simulation, *Weld. Int.* 10 (1996) 454–460. https://doi.org/10.1080/09507119609549030.

[4] D. J. Abson, J. S. Rothwell, Review of type IV cracking of weldments in 9–12 % Cr creep strength enhanced ferritic steels, *Int. Mater. Rev.* 58 (2013) 437–473. https://doi.org/10.1179/1743280412Y.0000000016.

[5] M. E. A. El-azim, A. M. Nasreldin, G. Zies, A. Klenk, Microstructural instability of a welded joint in P91 steel during creep at 600 u C, *Mater. Sci. Technol*. 21 (2005) 779–791. https://doi.org/10.1179/174328405X43216.

[6] S. K. Albert, M. Matsui, T. Watanabe, H. Hongo, K. Kubo, M. Tabuchi, Microstructural investigations on type IV cracking in a high Cr steel, *ISIJ Int.* 42 (2002) 1497–1504.

[7] T. Watanabe, M. Tabuchi, M. Yamazaki, H. Hongo, T. Tanabe, Creep damage evaluation of 9Cr-1Mo-V-Nb steel welded joints showing Type IV fracture, *Int. J. Press. Vessel. Pip*. 83 (2006) 63–71. https://doi.org/10.1016/j.jelectrocard.2005.07.009.

[8] S. K. Albert, M. Tabuchi, H. Hongo, T. Watanabe, K. Kubo, M. Matsui, Effect of welding process and groove angle on type IV cracking behaviour of weld joints of a ferritic steel, Sci. Technol. *Weld. Join*. 10 (2005) 149–157. https://doi.org/10.1179/174329305X36034.

[9] F. Abe, M. Tabuchi, F. Abe, M. Tabuchi, Microstructure and creep strength of welds in advanced ferritic power plant steels, *Sci. Technol. Weld. Join.* 9 (2004) 22–30. https://doi.org/10.1179/136217104225017107.

[10] J. A. Francis, W. Mazur, H.K.D.H. Bhadeshia, Estimation of Type IV Cracking Tendency in Power Plant Steels, *ISIJ Int*. 44 (2004) 1966–1968.

[11] K. Shinozaki, D. Li, H. Kuroki, H. Harada, K. Ohishi, T. Sato, Observation of type IV cracking in welded joints of high chromium ferritic heat resistant steels, *Sci. Technol. Weld. Join*. 8 (2003) 289–295. https://doi.org/10.1179/136217103225005444.

[12] M. E. Abd El-Azim, O. E. El-Desoky, H. Ruoff, F. Kauffmann, E. Roos, Creep fracture mechanism in welded joints of P91 steel, *Mater. Sci. Technol*. 29 (2013) 1027–1033. https://doi.org/10.1179/1743284713Y.0000000233.

[13] S. K. Albert, M. Matsui, T. Watanabe, H. Hongo, K. Kubo, M. Tabuchi, Variation in the type IV cracking behaviour of a high Cr steel weld with post weld heat treatment, *Int. J. Press. Vessel. Pip*. 80 (2003) 405–413. https://doi.org/10.1016/S0308-0161(03)00072-3.

[14] K. Sawada, M. Bauer, F. Kauffmann, P. Mayr, A. Klenk, Microstructural change of 9 % Cr-welded joints after long-term creep, *Mater. Sci. Eng.* A. 527 (2010) 1417–1426. https://doi.org/10.1016/j.msea.2009.10.044.

[15] T. Sato, K. Tamura, K. Mitsuhata, R. Ikura, Improvement of creep rupture strength of 9Cr1MoNbV welded joints by post weld normalizing and tempering, in: 5th *Int. Conf. Adv. Mater.* Technol., 2008: pp. 1–10.

[16] M. Dewitte, C. Coussement, Creep properties of 12 % Cr and improved 9 % Cr weldments, *Mater. High Temp*. 9 (1991) 178–184. https://doi.org/10.1080/09603409.1991.11689658.

[17] J. A. Francis, G.M.D. Cantin, W. Mazur, H.K.D.H. Bhadeshia, G.M.D. Cantin, W. Mazur, H.K.D.H. Bhadeshia, J.A. Francis, G.M.D. Cantin, W. Mazur, H.K.D.H. Bhadeshia, Effects of weld preheat temperature and heat input on type IV failure, *Sci. Technol. Weld. Join*. 14 (2009) 436–442. https://doi.org/10.1179/136217109X415884.

[18] M. Kondo, M. Tabuchi, S. Tsukamoto, F. Yin, F. Abe, M. Kondo, M. Tabuchi, S. Tsukamoto, F. Yin, F. Abe, Suppressing type IV failure via modification of heat affected zone microstructures using high boron content in 9Cr heat resistant steel welded joints, *Sci. Technol. Weld. Join*. ISSN. 11 (2006) 216–223. https://doi.org/10.1179/174329306X89260.

[19] V. L. Manugula, K. V. Rajulapati, G. M. Reddy, K.B.S. Rao, Role of evolving microstructure on the mechanical properties of electron beam welded ferritic-martensitic steel in the as-welded and post weld heat-treated states, *Mater. Sci. Eng. A.* 698 (2017) 36–45. https://doi.org/10.1016/j.msea.2017.05.036.

[20] William F. Newell JR., Welding and postweld heat treatment of P91 steels, *Weld.* J. 89 (2010) 33–36.

[21] M. Yamazaki, T. Watanabe, H. Hongo, M. Tabuchi, Creep rupture properties of welded joints of heat resistant steels, *Challenges Power Eng. Environ*. (2007) 1044–1048. https://doi.org/10.1299/jpes.2.1140.

[22] O. D. Sherby, E. M. Taleff, Influence of grain size, solute atoms and second-phase particles on creep behavior of polycrystalline solids, *Mater. Sci. Eng. A*. 322 (2002) 89–99. https://doi.org/10.1016/S0921-5093(01)01121-2.

[23] V. Dudko, A. Belyakov, D. Molodov, R. Kaibyshev, Microstructure evolution and pinning of boundaries by precipitates in a 9 pct Cr heat resistant steel during creep, *Metall. Mater. Trans. A Phys. Metall. Mater. Sci*. 44 (2013). https://doi.org/10.1007/s11661-011-0899-1.

[24] F. Abe, Creep rates and strengthening mechanisms in tungsten-strengthened 9Cr steels, *Mater. Sci. Eng. A.* 319–321 (2001) 770–773. https://doi.org/10.1016/S0921-5093(00)02002-5.

[25] T. Sakthivel, S.P. Selvi, K. Laha, An assessment of creep deformation and rupture behaviour of 9Cr-1.8W-0.5Mo-VNb (ASME grade 92) steel, *Mater. Sci. Eng. A.* 640 (2015) 61–71. https://doi.org/10.1016/j.msea.2015.05.068.

[26] J. Zhang, H. Di, Y. Deng, R.D.K. Misra, Effect of martensite morphology and volume fraction on strain hardening and fracture behavior of martensite-ferrite dual phase steel, *Mater. Sci. Eng. A.* 627 (2015) 230–240. https://doi.org/10.1016/j.msea.2015.01.006.

[27] M. I. Isik, A. Kostka, G. Eggeler, On the nucleation of Laves phase particles during high-temperature exposure and creep of tempered martensite ferritic steels, *Acta Mater.* 81 (2014) 230–240. https://doi.org/10.1016/j.actamat.2014.08.008.

[28] W. Liu, X. Liu, F. Lu, X. Tang, H. Cui, Y. Gao, Creep behavior and microstructure evaluation of welded joint in dissimilar modified 9Cr-1Mo steels, *Mater. Sci. Eng. A.* 644 (2015) 337–346. https://doi.org/10.1016/j.msea.2015.07.068.

[29] K. Shinozaki, D.-J. Li, H. Kuroki, H. Harada, K. Ohishi, Analysis of Degradation of Creep Strength in Heat-affected Zone of Weldment of High Cr Heat-resisting Steels Based on Void Observation., *ISIJ Int.* 42 (2002) 1578–1584. https://doi.org/10.2355/isijinternational.42.1578.

[30] K. Miyahara, J. H. Hwang, Y. Shimoide, Aging phenomena before the precipitation of the bulky laves phase in Fe-10 %Cr ferritic alloys, *Scr. Metall. Mater.* 32 (1995) 1917–1921. https://doi.org/10.1016/0956-716X(95)00086-B.

[31] X Z. Zhang, X. J. Wu, R. Liu, J. Liu, M. X. Yao, Influence of Laves phase on creep strength of modified 9Cr-1Mo steel, *Mater. Sci. Eng. A.* 706 (2017) 279–286. https://doi.org/10.1016/j.msea.2017.08.111.